A Critical Review of Orificed Hollow Cathode Modeling: 0-D Models

Christopher J. Wordingham,* Pierre-Yves C. R. Taunay,*

Edgar Y. Choueiri†

Princeton University, Princeton, NJ, 08544, USA

A critical review of zero-dimensional orificed hollow cathode modeling is presented, with a focus on the validity of model assumptions, the reproducibility of model results, and the observed scaling behaviors. Complete models were capable of recreating the original results of their authors, but were generally unable to produce agreement with other experimental data. Resolution of the potential structure of the emitter sheath beyond the inclusion of the pre-sheath is attempted in only one model. In all other models it is assumed that the plasma and sheath potentials are equal, inflating the contribution of emitter ion bombardment and power deposition in the insert plasma by sheath electrons while essentially neglecting electron back-bombardment. Model results are generally sensitive to the internal neutral pressure, but neutral flow predictions do not agree with experimental data. Inconsistent property data and the inappropriate evaluation of flux terms between control volumes are pervasive, and introduce significant errors. Most models require substantial input in the form of experimental data or free parameters and cannot be used for predictive calculations.

List of Symbols

Constants		
ϵ_0	Permittivity of vacuum	8.85×10^{-12} F/m
C_0	Double sheath factor	1.8516
e	Elementary charge	1.602×10^{-19} C
h	Planck's constant	6.62×10^{-34} J·s
k_B	Boltzmann's constant	1.38×10^{-23} J/K
m	Electron mass	9.1×10^{-31} kg
Circuit parameters		
I_d	Discharge current	A
R_p	Plasma resistance	Ω
R_{or}	Orifice plasma resistance	Ω
V_d	Discharge voltage	V
Geometry		
A_{emit}	Emitter area	m^2
L_{emit}	Emission length	m
L_i	Insert length	m
L_o	Orifice length	m
L_t	Cathode tube length	m
L_{ck}	Cathode tip to keeper length	m
r_c	Cathode (insert) radius	m
r_o	Orifice radius	m
r_{ci}	Cathode tube inner radius	m
r_{ds}	Spherical double sheath radius	m
t_c	Cathode tube thickness	m
t_i	Insert thickness	m
Plasma parameters		
α	Ionization fraction	
η_p	Plasma resistivity	Ω·m

*Graduate Student, MAE Dept., Princeton University, AIAA Student Member.

†Chief Scientist, EPPDyL, Professor, Applied Physics Group, MAE Dept., Princeton University, AIAA Fellow.

ϕ_p	Plasma potential	V
ϕ_s	Sheath potential	V
ϕ_{ds}	Double sheath potential	V
ϕ_{ps}	Pre-sheath potential	V
D	Diffusion coefficient	m^2/s
D_a	Ambipolar diffusion coefficient	m^2/s
I_e	Electron current	A
I_i	Ion current	A
I_r	Random electron current	A
I_{em}	Thermionic current	A
J_e	Electron current density	A/m^2
J_r	Random electron current density	A/m^2
J_{em}	Thermionic current density	A/m^2
J_i	Ion current density	A/m^2
n_e	Electron density	m^{-3}
n_g	Neutral gas density	m^{-3}
N_i	Total number of ions	
n_i	Ion density	m^{-3}
N_{ex}	Total number of excited atoms	
T_e	Electron temperature	K
T_g	Neutral gas temperature	K
T_i	Ion temperature	K
T_{eV}	Electron temperature	V
T_{gV}	Neutral gas temperature	V
T_{iV}	Ion temperature	V
v_B	Bohm velocity	m/s

Collisions

λ_{ex}	Mean free path for excitation	m
λ_{pr}	Energy exchange mean free path	m
ν_{ei}	Electron-ion collision frequency	s
ν_{en}	Electron-neutral collision frequency	s
ν_{in}	Ion-neutral collision frequency	s
σ_{CEX}	Charge-exchange cross section	m^2
σ_{en}	Electron-neutral collision cross section	m^2
σ_{ex}	Excitation cross section	m^2
σ_{in}	Total inelastic cross section	m^2
σ_{iz}	Ionization cross section	m^2

Thermionic emission

ϕ_{eff}	Effective work function	V
ϕ_w	Surface work function	V
D_{RD}	Richardson-Dushman constant	$A/(m^2 \cdot K^2)$
E_c	Cathode surface electric field	V/m

Power terms

$\dot{q}_{\mathrm{conv}}$	Convection power	W
$\dot{q}_\Omega$	Resistive power	W
$\dot{q}_{\mathrm{coll}}$	Power lost to plasma volume by random electron flux	W
$\dot{q}_{\mathrm{ori}}$	Power deposited in plasma volume by orifice ions	W
$\dot{q}_{dx}$	Power deposited at insert surface by de-excitation of excited states	W/m^2
$\dot{q}_{em}$	Power deposited in plasma volume by thermionic electrons	W
$\dot{q}_{ex}$	Excitation power	W
$\dot{q}_{iz}$	Ionization power	W
$\dot{q}_{ph}$	Power deposited at insert surface by emitted photons	W/m^2
$\dot{q}_{th}$	Thermal power lost from the insert	W

Gas properties

ϵ_i	Ionization energy	eV
ϵ_{ex}	Excitation energy	eV
μ	Dynamic viscosity	Pa·s
d_m	Diameter of particles as hard-spheres approach	m
M	Ion or neutral particle mass	kg

Flow properties

$\dot{m}$	Mass flow rate	kg/s
γ	Ratio of heat capacities	
P	Total pressure	Pa
P_g	Neutral gas pressure	Pa
R	Gas constant	J/(kg·K)

Other symbols

δ	Free parameter for Mizrahi *et al.* model	Σ_i	Internal partition function for the singly ionized state
λ_{01}	First zero of 0-th Bessel function of the first kind	τ_{ij}	Ratio of the temperature T_i to T_j
Σ_0	Internal partition function for the neutral state	T_c	Cathode wall temperature K
		T_o	Orifice plate temperature K

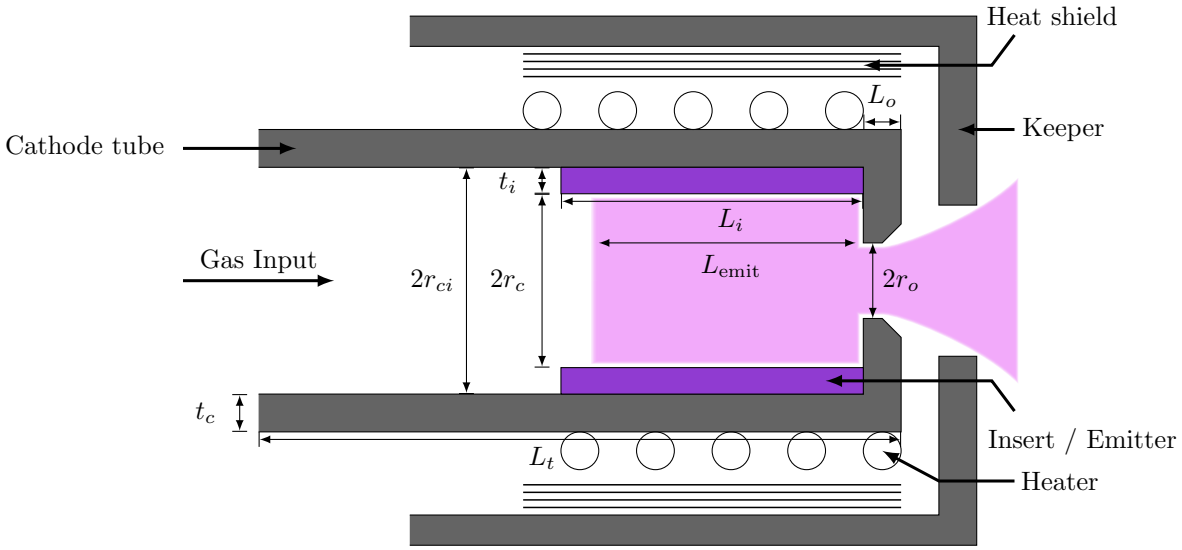

Figure 1. Orificed hollow cathode schematic.

I. Introduction

Modern Hall and ion thrusters rely on orificed hollow cathodes as neutralizers and plasma generators in order to provide the required neutralization and/or discharge currents while operating efficiently (at low voltage due to the high internal pressure, and at low mass flow rates compared to similarly sized single-channel hollow cathodes) with long operational life. Discharge power and lifetime requirements for Hall and ion thrusters continue to increase, while "near-term" projected power throughput for next-generation thrusters is expected to be $100 - 200$ kW,[1] with some proposed missions requiring operational lifetimes of up to 100 kh.[2,3] For specific impulses in the range of $2000 - 6000$ s, cathode discharge currents approaching 700 A may be required.[4,5] At least one existing Hall thruster has already been designed to operate at up to 200 kW,[6] and an accompanying hollow cathode has been developed by Goebel *et al.*[5] in order to provide the expected 300 A of discharge current required with an estimated operational life of $10 - 20$ kh. In our own work,[7] we have demonstrated a large hollow cathode capable of providing up to 400 A of discharge current, but without probe measurements of the plasma potential, emitter temperature profile, or internal axial plasma density profile, the expected operational life cannot be predicted accurately. Lower-current hollow cathodes have already demonstrated life tests up to 50 kh,[8] but experimental verification of operational life is costly and extremely time-consuming. In order to continue the development of long-life, high-discharge-current orificed hollow cathodes, generally applicable cathode models that provide predictive capabilities without requiring preexisting experimental measurements will be a necessity.

Several approaches have been used to model the physical processes within orificed hollow cathodes, often restricting their focus to the "active zone" or insert plasma region[9–11] where significant electron emission is supplied to the plasma by the emitter, generating sufficient ion current from the plasma to be self-sustaining and to avoid space-charge-limited emission. The insert plasma is usually modeled with either 0-D or 2-D axisymmetric approaches, either including the orifice as a coupled region or using a separate model implemented as a boundary condition. This review examines 0-D approaches to orificed cathode modeling.

The 0-D approach relies on a control volume with volume-averaged plasma properties. While important processes such as the variation of the plasma density along the cathode axis or the plasma potential along its radial direction may be neglected, 0-D models can still provide useful results and scaling relationships. Any choice of simulation dimension requires the inclusion of plasma-wall interactions for a comprehensive model, ideally implemented in the form of a double- or emitting-sheath model at the surface of the emitter. The emission mechanism is typically assumed to be field-enhanced thermionic emission,[12–14] governed by the Richardson-Dushman equation. The work function is often modified to account for the Schottky effect due to the sheath electric field (though this correction is sometimes neglected[11]). In order to estimate the electric field at the emitter surface, the double-sheath analysis of Prewett and Allen[15] is typically employed using the plasma potential instead of the sheath potential; the effect of this simplification will be discussed in later sections. Other important emission processes, such as space-charge-limited emission, are often ignored or implicitly handled through the use of the emission length or "active zone" where the plasma density is assumed to be sufficient to avoid limitation of the extracted thermionic current.

One of the primary difficulties associated with the assumption of uniform plasma properties is that it requires a description of the appropriate boundaries of the active zone in order to model the insert emission region. The calculation of the emission length, L_{emit}, or active zone length, in the axial direction typically requires a separate model, as the 1-D variation of the plasma and neutral densities appears to govern the formation of this region.

Approaches for calculating the attachment length include: 1) using a fixed multiple of the mean free path for energy exchange[10,16] of the emitted electrons, 2) assuming ambipolar-diffusion-dominated density decay,[11] 3) using empirical correlations that yield L_{emit} as a function of the cathode internal pressure,[14] 4) iterative calculations of the discharge power (selecting L_{emit} such that the power is minimized),[9] 5) using L_{emit} as a free parameter to fit experimental data,[14] or 6) taking L_{emit} from experimental data.[11]

While various models have been proposed, few are completely self-consistent or self-contained and readily available to extend the domain of operation of hollow cathodes. This paper will review 0-D models developed since the advent of the orificed hollow cathode, summarize the necessary inputs and expected outputs of each model, and provide critical insight on their quality and validity. The resulting analysis is given in Section II. When possible, the results of the original authors are re-implemented using Python and its Numpy[17] and Scipy[18] packages and shown following the model description and review. Non-linear systems of equations are solved in a least squares approach with Scipy's `root` solver configured with the Levenberg-Marquardt algorithm.[19] Comparisons between the various model results and experimental data for two benchmark cathodes are given in Section III. Finally, the critical modeling issues we identified in our review are discussed in Section IV and our conclusions are given in Section V.

II. Model Review

A. Siegfried and Wilbur[20]

A simple first-principles approach was initially chosen by Siegfried and Wilbur to model orificed hollow cathodes operating on mercury, employing tantalum-foil inserts coated with the low work function material R-500 (ϕ_w of approximately 2.3-2.4 eV). Their work follows modeling efforts from Bessling.[21] Plasma-wall interactions are entirely neglected in this model, but it allows for the calculation of the local plasma density and ionization fraction as a function of the measured electron temperature and the — calculated or measured — cathode pressure. The cathode stagnation pressure is estimated assuming choked-sonic flow at the orifice,

$$P = \frac{\dot{m}\sqrt{T_g}}{\pi r_o^2}\left[\frac{\gamma}{R}\left(\frac{2}{\gamma+1}\right)^{\frac{\gamma+1}{\gamma-1}}\right]^{-1/2}, \tag{1}$$

where P and T_g are stagnation quantities. Using the set input mass flow rate for $\dot{m}$ in Equation 1 implicitly assumes that 100% of the propellant gas leaves the cathode in a neutral state, and therefore neglects ionization processes that decrease the total number density of neutrals as well as any pressure contributions from plasma ions or electrons. It also neglects viscous effects within the orifice and insert region and the heating of the neutral gas by the plasma, as the derivation of Equation 1 relies on the assumption of isentropic flow. The effect of the discharge current on the pressure is also neglected, though the authors note that the variation was only 15% of the total over the range of discharge currents examined. Siegfried and Wilbur also report

good agreement between measured and calculated pressures, despite the apparent inapplicability of the flow model used.

The ionization fraction α is determined based on a two-temperature Saha model,

$$\frac{\alpha^{1+\tau_{ge}}}{(1-\alpha)^{\tau_{ge}}\left(1+\alpha/\tau_{ge}\right)} = \frac{1}{P}\frac{(2\pi m)^{3/2}}{h^3}e^{5/2}T_{gV}T_{eV}^{3/2}\left(\frac{\Sigma_i}{\Sigma_0}\right)^{\tau_{ge}}\exp\left(-\frac{\epsilon_i}{T_{eV}}\right), \tag{2}$$

where $\alpha = n_e/\left(n_e + n_g\right)$, the total pressure is expressed in Pascals, and the ions/neutrals are assumed to be in thermal equilibrium with one another, but not with the electrons, which are further assumed to have equilibrated amongst themselves. The total pressure is linked to the heavy particle density and plasma density using the perfect gas law

$$P = e\left(n_e T_{eV} + n_g T_{gV} + n_i T_{iV}\right), \tag{3}$$

assuming that the densities and temperatures are uniform within the cathode. The neutral temperature is also assumed to be equal to the ion temperature and is calculated as the average of the estimated internal cathode temperature and the orifice plate temperature (≈ 0.1 eV for Siegfried and Wilbur's experiment).

Algorithm If the measured pressure is not available, the cathode stagnation pressure should first be calculated using Equation 1 and the input mass flow rate. If the cathode stagnation (upstream) pressure has been measured, this value can be used directly in Equation 2 along with the measured electron temperature to find the ionization fraction. Equation 3 is then used to obtain the electron density.

Evaluation The authors demonstrate good agreement between calculated and experimental data for their mercury cathode operating in spot mode ($I_d = 6.0$A at $\dot{m} = 100$mA). In plume mode ($I_d = 2.0$A at the same $\dot{m}$), the authors experimentally measured a flat electron temperature profile, but chose to use a linear fit for the electron temperature when implementing their model as it gives better agreement with the experimental data. Siegfried and Wilbur also demonstrate that the model results are sensitive to the chosen neutral gas temperature. They compare the results of the algorithm for two values of T_{gV}: T_{gV}=0.1 eV and $T_{gV} = T_{eV}$. The latter value results in an increase in the ionization fraction, and therefore the plasma density, of several orders of magnitude.

We have implemented Siegfried and Wilbur's solution using the measured electron temperature and cathode pressure data that they report. Results are shown in Fig. 2. We obtain good agreement with the original work by Siegfried and Wilbur.

B. Siegfried and Wilbur[10,12,16,22,23] — a refined approach

Siegfried and Wilbur refined their original model in a series of articles and reports. In this refined model, the authors assume that the plasma properties are uniform within an "ion production region" which coincides with the insert emission area (or attachment length, L_{emit}). An early version of the new model is described in Refs. 12 and 22. It consists of a current balance and insert power balance, with the assumption that ions are either collected at the emitter or the orifice plate, leave the cathode through the orifice, or travel toward the upstream region of the cathode at the Bohm velocity. The sheath electric field is described using Child's law and an assumed sheath thickness of one Debye length (thereby assuming a single-species, space-charge-limited sheath). The unknowns of this system are the plasma potential, electron temperature, emitter temperature, and plasma density. This version of the model requires two measured quantities (electron temperature and plasma potential), the emission length, and the heat loss from the emitter (through conduction, radiation, and convection) in order to solve for the two other quantities of interest. This model is still a notable improvement over the initial one, as it does not rely on a Saha-type equation for the ionization fraction, the use of which is generally not justified.[9,14]

A later, improved approach introduced a flow model, a double-sheath approach to treat the electric field at the cathode surface, and a plasma volume power balance. The emission length is linked to the energy-exchange mean free path of the emitted electrons. The introduction of two additional physical constraints allows for four physical quantities to be computed — the plasma density, plasma potential, neutral gas density, and emitter temperature. The electron temperature remains a free parameter. This improved version is described and critiqued below.

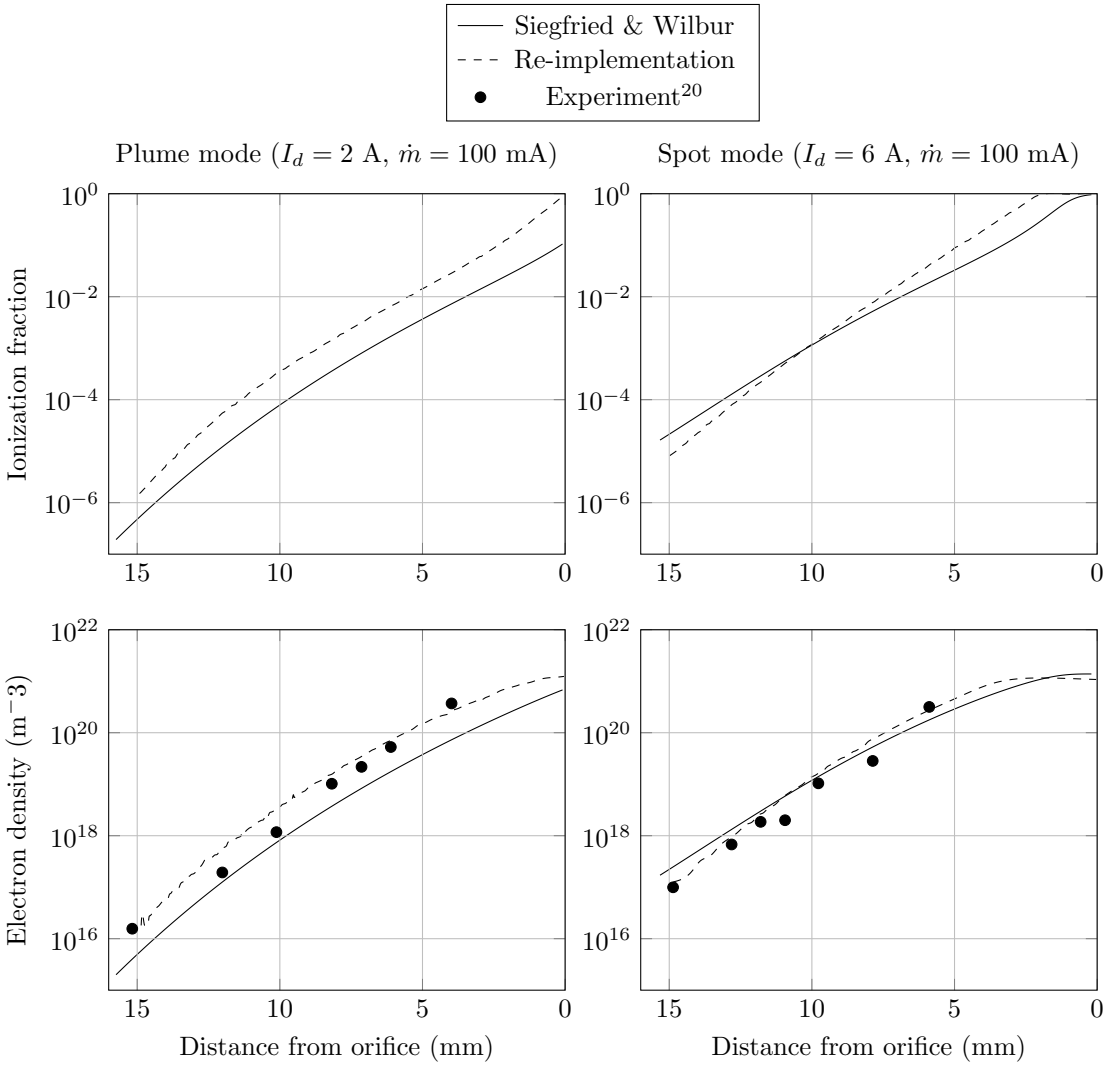

Figure 2. Comparison of ionization fraction and electron density as calculated with Siegfried and Wilbur's original model (Ref. 20, dashed lines) and our re-implementation (solid lines). Experimental data from Ref. 20 is included; it does not feature error bars. Two test cases are considered for a mercury hollow cathode.

MODEL DETAILS The cathode pressure upstream of the orifice is assumed to be equal to the stagnation pressure, which is roughly constant along the cathode length. It is given by an empirical relationship,

$$P = \left(\frac{\dot{m}}{4r_o^2}\right)(c_1 + c_2 I_d) \times 10^{-3}, \tag{4}$$

where P is in Torr, $\dot{m}$ in mA-equivalent, and r_o in mm. The constants c_1 and c_2 depend on the gas of interest. Equation 4 addresses the shortcomings of Equation 1, as it is empirically derived and does not neglect the effects of the plasma on the flow.

Ion and electron currents are related to the total discharge current through a net current balance. Ions are lost from the plasma volume at the emitter and orifice boundaries and in the upstream portion of the cathode. Siegfried and Wilbur assume that the ions are lost upstream at the Bohm velocity, as opposed to the ion thermal velocity. This leads to an ion current contribution approximately 2 times higher at the upstream boundary as compared to the ion thermal current (using $T_{eV} = 0.8$ eV and $T_{iV} = 0.1$ eV).

$$I_d = I_e + I_i = J_{em} A_{\text{emit}} + J_i \left(A_{\text{emit}} + 2\pi r_c^2\right) \tag{5}$$

The ion current is obtained with the Bohm velocity, which is assumed to be valid even with a boundary emitting electrons, a common assumption that yields reasonable results (the modification of the Bohm velocity is expected not to exceed approximately 20% of the assumed value) but that is not entirely justified. The effect of the pre-sheath on the ion density is also neglected in the expression for the ion current density:

$$J_i = e n_e \left(\frac{e T_{eV}}{M}\right)^{1/2}. \tag{6}$$

It is assumed that no electrons return to the insert from the plasma so that only thermionic electrons contribute to the total current, in sharp contrast with later models.[11,14,24] This assumption does not hold under all conditions encountered in orificed hollow cathodes. Assuming that the collection areas for back-streaming electrons and ions are the same, the ratio of back-streaming electrons to ion current at the insert surface may be calculated as

$$\frac{I_r}{I_i} = \left(\frac{M}{2\pi m}\right)^{1/2} \exp\left(-\phi_s / T_{eV}\right). \tag{7}$$

Fig. 3 illustrates this ratio for common operating conditions found in orificed hollow cathodes, for both mercury and xenon as propellant. For the case where the sheath potential is taken to be equal to the plasma potential, this assumption may be valid at low electron temperatures (1–1.5 eV).

The Richardson-Dushman relationship is used to calculate the thermionic current,

$$J_{em} = D_{RD} T_c^2 \exp\left(-\frac{e\phi_{\text{eff}}}{k_B T_c}\right), \tag{8}$$

with an effective work function modified to take into account the finite electric field at the cathode surface,

$$\phi_{\text{eff}} = \phi_w - \left(\frac{e\,|E_c|}{4\pi\epsilon_0}\right)^{1/2}. \tag{9}$$

The cathode surface electric field can be calculated using an approximate form of the surface electric field expression from Prewett and Allen's double sheath model:[15]

$$E_c \approx \left(\frac{n_e e T_{eV}}{\epsilon_0}\right)^{1/2} \left(2\left(1 + 2\frac{\phi_p}{T_{eV}}\right)^{1/2} - 4\right)^{1/2}. \tag{10}$$

Siegfried and Wilbur use the plasma potential instead of the sheath potential in Equation 10. The correction to the work function is not affected by this change, as the plasma potential only appears to the 1/4-th power in Equation 9

The model includes power balances for both the insert surface and plasma volume, given by Equations 11 and 12, respectively. Power deposition to the insert by de-excitation and photon absorption are neglected,

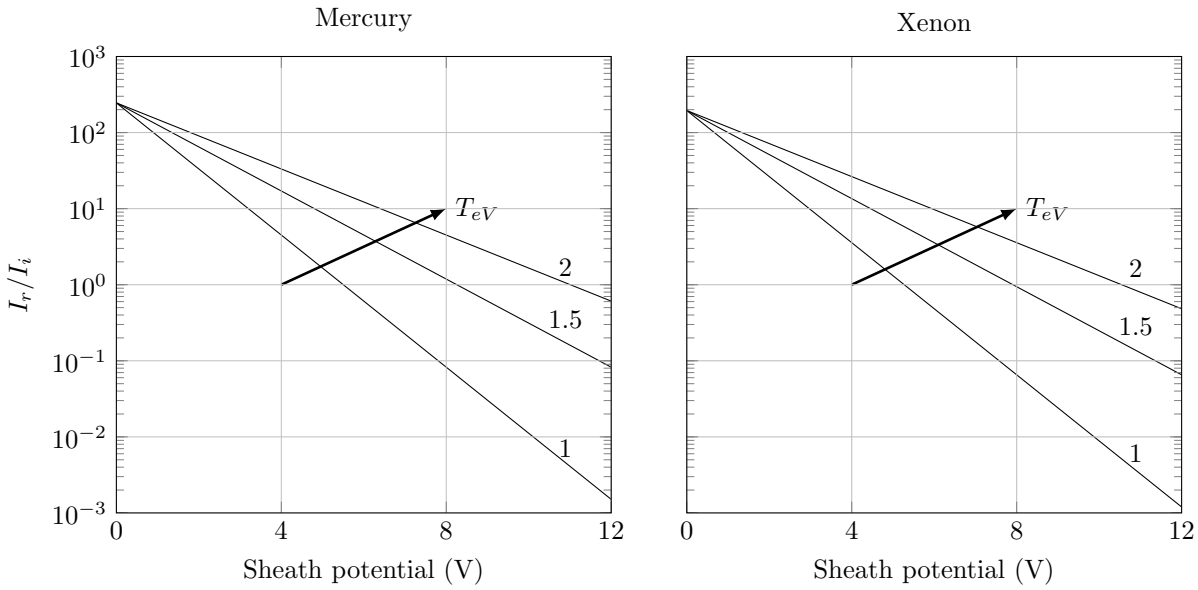

Figure 3. Ratio of thermal electron current to ion current for varying sheath potentials and electron temperatures. Left: mercury. Right: xenon.

as shown below.

$$J_i A_{\text{emit}} \left(\phi_p + \epsilon_i - \phi_w\right) + \underbrace{\dot{q}_{dx} A_{\text{emit}} + \dot{q}_{ph} A_{\text{emit}}}_{\text{neglected}} = \dot{q}_{th} + I_{em}\phi_{\text{eff}} \tag{11}$$

$$\phi_p I_e = \epsilon_i I_i + \frac{5}{2} T_{eV} I_d \tag{12}$$

Ohmic heating in the plasma is ignored, which becomes more significant with increasing discharge current. The electrons back-streaming to the surface are neglected here as well. The power contribution of the backstreaming electrons may be compared to the ion contribution

$$\frac{P_r}{P_i} = \left(\frac{M}{2\pi m}\right)^{1/2} \exp\left(-\phi_s/T_{eV}\right) \frac{2T_{eV} + \phi_w}{\epsilon_i + \phi_s - \phi_w}. \tag{13}$$

Fig. 4 illustrates the power ratio for common operating conditions found in orificed hollow cathodes, for mercury and xenon propellants. Similar conclusions to those drawn from Fig. 3 can be reached: assuming a sheath potential equal to the plasma potential (usually 8–12 V) and low electron temperature justifies neglecting the random electron flux.

The plasma attachment length is taken to be proportional to the energy-exchange mean free path of the thermionically emitted electrons (primary electrons):

$$L_{\text{emit}} = c_3 \lambda_{pr}, \tag{14}$$

where c_3 varies with the gas species.[16] The energy-exchange mean free path is the mean free path of the primary electrons. For mercury, it may be estimated with

$$\lambda_{pr} = \left(\frac{6.5 \times 10^{-17} n_e}{\phi_p^2} + \frac{10^3 n_g \phi_p}{2.83 \times 10^{23} - 1.5 n_g}\right)^{-1}, \tag{15}$$

where the first term corresponds to elastic collisions, while the second approximates inelastic collisions. Only electron-electron collisions are retained for elastic collisions, as they dominate over electron-atom and electron-ion elastic collisions.[23] In Equation 15, the second term is a fit to Peters and Wilbur's model, as the knowledge of the density of every gas state needs to be known. For other species, the inelastic mean

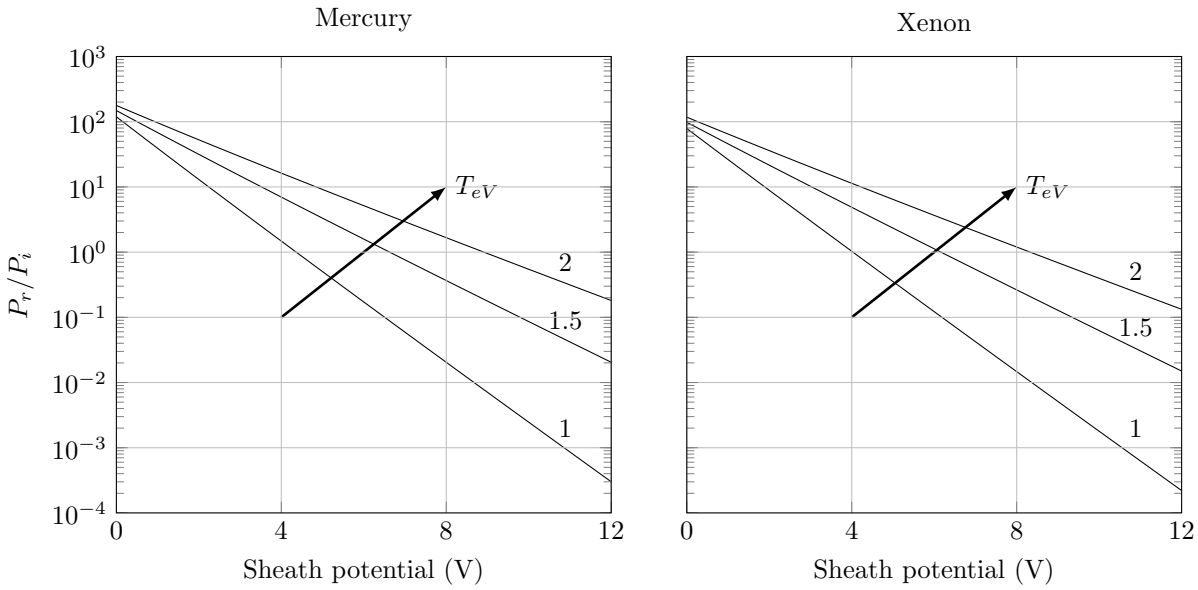

Figure 4. Ratio of the contribution to the insert surface power balance from thermal electrons and ions for varying sheath potentials and electron temperatures. Left: mercury. Right: xenon.

free path can be estimated using its usual definition with the plasma potential taken as the electron beam energy

$$\lambda_{pr} = \left(\frac{6.5 \times 10^{-17} n_e}{\phi_p^2} + n_g \sigma_{in} \left(\phi_p \right) \right)^{-1}. \tag{16}$$

The total inelastic collision cross section includes excitation and direct ionization reactions, both from ground states, but step-wise ionization is ignored. The system is closed with the perfect gas law (Equation 3).

The final version of the model still relies on experimental data, as it does not include any prediction of the electron temperature. The heat loss is calculated by considering surface-to-ambient radiation and conduction through the cathode back to the cathode base. Several other noteworthy assumptions and simplifications exist in all versions of the model, including:

- Except in the calculation of the energy-exchange mean free path for mercury, excitation and stepwise ionization are ignored. This is a common assumption[11,14] that appears to produce decent results despite being generally unjustified.
- As a result of the assumption that plasma and sheath potentials are equal, the energy of the primary electrons for use in calculating the energy-exchange mean free path is assumed equal to the plasma potential, which may differ from the energy the electrons would actually gain in the sheath.

Algorithm Based on the operational points for discharge current or pressure (I_d or P), the cathode geometry (r_o, r_c), emitter material (ϕ_w), the propellant of interest (ϵ_i, M), electron temperature T_{eV}, and heat loss term $\dot{q}_{th}$, the four physical Equations 3, 5, 11, and 12 are solved for the electron density, neutral gas density, plasma potential, and insert temperature. The constants c_1, c_2, and c_3 may be found in Ref. 16 (included them in the Appendix).

Evaluation For a mercury cathode, the model shows relatively good agreement for the evolution of the emitter temperature as a function of discharge current, and plasma density as a function of internal pressure. However, the model predicts a non-linear trend for the plasma density as a function of discharge current, in contradiction with experimental data. The predicted plasma density evolves linearly as a function of the internal pressure and does not capture the saturation of the plasma density for pressures above 3 Torr. The model also tends to under-predict the plasma potential for the mercury cathode, with the caveat that it is only compared to a single value for a different experiment. Results of the model are shown in Fig. 5, along

with a comparison with our implementation of this model. Calculations for the xenon cathode are shown later in comparisons with other models.

In summary, the various incarnations of Siegfried and Wilbur's model can produce good agreement with experimental data, but cannot predict the electron temperature and require an additional model for the insert heat loss, in addition to relying upon a number of assumptions that may not hold for other cathode operating conditions.

C. Mandell and Katz[25–28]

Mandell and Katz offer a model of the orifice plasma only. It relies on the balance of ion production and losses, a neutral gas flow model, and a plasma power balance.

NEUTRAL GAS FLOW From mass conservation, the total mass flow rate is equal to the sum of the gas and ion mass flow rates:

$$\dot{m} = \dot{m}_g + \dot{m}_i. \tag{17}$$

In units of equivalent-Ampères, the mass flow rates have the following form:

$$\dot{m}_g = \pi r_o^2 n_g e \sqrt{\frac{eT_{gV}}{2\pi M}} \tag{18}$$

$$\dot{m}_i = \pi r_o^2 J_i. \tag{19}$$

The ion current density is defined using the average velocity of a Maxwellian distribution:

$$J_i = n_e e \sqrt{\frac{eT_{iV}}{2\pi M}}. \tag{20}$$

ION BALANCE The ion production through direct electron-impact ionization is balanced by the losses to the boundaries of the system

$$\left(\frac{dN_i}{dt}\right)_{\text{iz}} = \left(\frac{dN_i}{dt}\right)_{\text{out}}. \tag{21}$$

The ionization rate is estimated using a Maxwellian-averaged cross-section:

$$\left(\frac{dN_i}{dt}\right)_{\text{iz}} = \left(\pi r_o^2 L_o\right) n_e n_g \sigma_{iz}(T_{eV}) \sqrt{8\frac{eT_{eV}}{\pi m}}. \tag{22}$$

For xenon, the ionization cross-section is calculated with a fit to Hayashi's experimental data[29]

$$\sigma_{iz}(T_{eV}) = \left(3.97 + 0.643T_{eV} - 0.0368T_{eV}^2\right) \exp\left(\frac{-12.127}{T_{eV}}\right) \times 10^{-20}. \tag{23}$$

Ion losses occur through the boundaries of the orifice. Mandell and Katz assume that the ion losses are uniform at the orifice entrance, exit, and walls. Neglecting the density and potential drop due to the pre-sheath, and using the thermal flux for ion loss, the ion outflow is given by:

$$\left(\frac{dN_i}{dt}\right)_{\text{out}} = 2\pi r_o \left(r_o + L_o\right) \sqrt{\frac{eT_{eV}}{2\pi M}} n_e. \tag{24}$$

PLASMA POWER BALANCE Ohmic heating is balanced by ionization, radiation / excitation, and convection losses.

$$\dot{q}_\Omega = \dot{q}_{iz} + \dot{q}_{ex} + \dot{q}_{\text{conv}} \tag{25}$$

$$\Leftrightarrow R_p I_d^2 = \left(\frac{dN_i}{dt}\right)_{\text{iz}} \langle \epsilon_i \rangle + \left(\frac{dN_i}{dt}\right)_{\text{ex}} \langle \epsilon_{ex} \rangle + I_d \left(T_{eV} - T_{eV}^{\text{ins}}\right), \tag{26}$$

where $\left(\frac{dN_i}{dt}\right)_{\text{ex}}$ has the same expression as $\left(\frac{dN_i}{dt}\right)_{\text{iz}}$, with the excitation cross-section substituted for the ionization cross-section. For xenon, the excitation cross-section can be fit to Hayashi's experimental data:

$$\sigma_{ex}(T_{eV}) = 1.93 \times 10^{-19} T_{eV}^{-1/2} \exp\left(\frac{-11.6}{T_{eV}}\right). \tag{27}$$

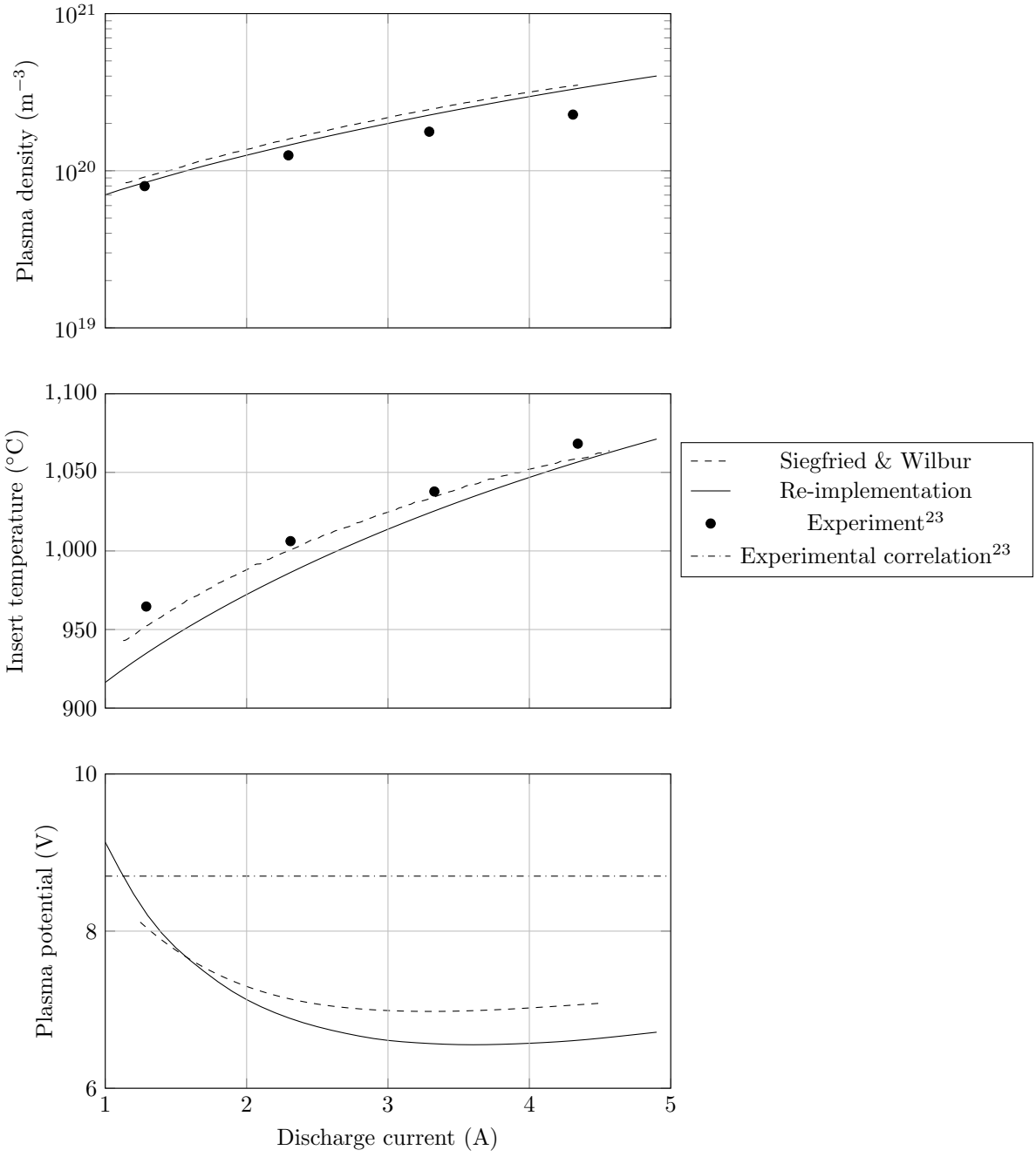

Figure 5. Comparison of electron density, cathode wall temperature, and plasma potential as calculated with Siegfried and Wilbur's refined model (Ref. 10, 12, 23, dashed lines) and our re-implementation (solid lines). Experimental data from Ref. 23 is included; error bars are not provided.

The average ionization and excitation energies are estimated as 12.2 eV and 10 eV, respectively. The authors have omitted the factor of 5/2 for the convection losses in Equation 25.

The plasma resistivity contains contributions from both electron-ion and electron-neutral collisions, and is given by:

$$\eta_p = \frac{m}{n_e e^2} \left(\nu_{ei} + \nu_{en} \right). \tag{28}$$

The plasma resistance is obtained from the resistivity and the orifice geometry assuming axial current conduction:

$$R_p = \eta_p \frac{L_o}{\pi r_o^2} \tag{29}$$

The electron-ion collision frequency is obtained using:

$$\nu_{ei} = 2.9 \times 10^{-12} n_e \ln \Lambda T_{eV}^{-3/2}, \tag{30}$$

with the Coulomb logarithm expressed as

$$\ln \Lambda = 30 - \frac{1}{2} \ln \left(n_e T_{eV}^{-3} \right). \tag{31}$$

The electron-neutral collision frequency may be defined with a hard-sphere model with a constant collision cross-section equal to 5×10^{-19} m^2 (e.g., Ref. 25). Alternatively, it may be calculated based on the momentum transfer cross-section. The authors propose a fit to experimental cross-section data:[28]

$$\sigma_{en} = 6.6 \times 10^{-19} \frac{T_{eV}/4 - 0.1}{1 + (T_{eV}/4)^{1.6}}, \tag{32}$$

but use the total electron-neutral collision cross-section, which also includes inelastic collisions, instead of the momentum transfer cross-section. Fig. 6 features a comparison of the fit to the total, Maxwellian-averaged, experimental cross-section, and to the Maxwellian-averaged momentum-transfer cross-section, both from Hayashi's experimental data.[29] Equation 32 approximates Hayashi's recommended data for the total electron-neutral collision cross-section for electron temperatures between 1 and 10 eV (Fig. 6, left). The numerical fit also approximates the momentum-transfer cross-section for electron temperatures between 0.8 and 2 eV. However, the fit overestimates momentum-transfer data by a factor of 2 for electron temperatures above 2 eV. More recent elastic electron-neutral cross-section data also indicates that Equation 32 underestimates the electron-neutral cross-section at low electron energies (Fig. 6, right). We retrieved the elastic cross-section data from the LXCAT website[30] (originally from Ref. 31). We recommend using the more recent elastic cross-section data from Hayashi to estimate the electron-neutral collision frequency.

Further assumptions are required to compute the plasma density, neutral gas density, and electron temperature. The authors assume that:

- The ion temperature is equal to the electron temperature. This is in sharp contrast with both earlier[10,12,20,23] and later models,[11] where the ion temperature is set equal to the neutral gas temperature, a consequence of frequent charge-exchange collisions in the plasma volume. The authors relax this assumption in Ref. 28, and set T_{iV} equal to 0.1 eV.
- The electron temperature from the insert T_{eV}^{ins} is known.
- The neutral gas temperature is known.

Algorithm The ion balance (Equation 21), plasma power balance (Equation 25), and mass conservation (Equation 17) are solved iteratively. The orifice geometry (r_o , L_o), gas properties (ϵ_i , ϵ_{ex} , σ_{iz} , σ_{ex} , σ_{en} , M), and operating conditions (I_d , $\dot{m}$) are required inputs.

Evaluation The neutral gas temperature is assumed to be equal to that of the wall of the cathode studied in Ref. 25, and set to 0.1 eV. The insert electron temperature is not specified or reported in the test cases presented in Refs. 25–28. It is possible to infer this quantity from Equations 17, 21, and 25. Using values reported in Ref. 25, we calculated T_{eV}^{ins}. Results are shown in Fig. 7. We used an average value of $T_{eV}^{\text{ins}} = 0.8$ eV for the rest of our calculations.

We were able to reproduce the model described above. Results are shown in Fig. 8. The original authors do not compare the results of this cathode model to experimental data. Our re-implementation of this model features excellent agreement with the original results.

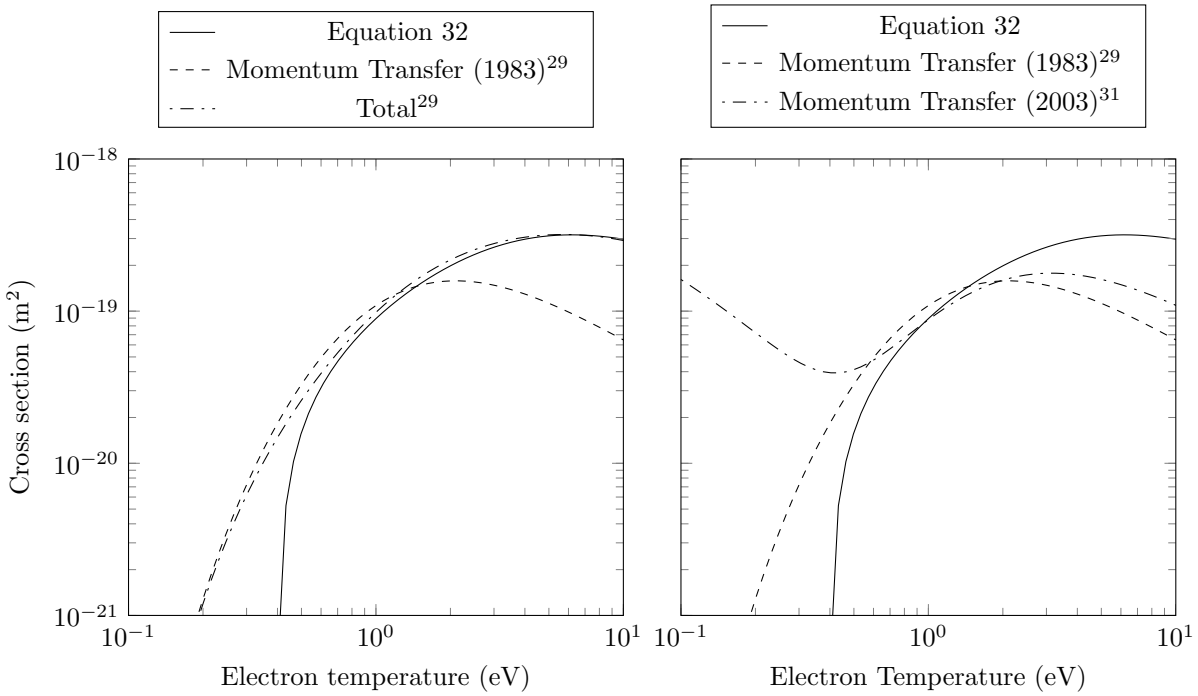

Figure 6. Left: Comparison of Katz's fit (Equation 32) to Hayashi's recommended data for total electron-neutral collision cross-section, and to the electron-neutral elastic collision cross-section (Ref. 29). Right: Comparison of Katz's fit to elastic collision cross-section for momentum-transfer, for two experimental data sets. The reported cross-sections are Maxwellian-averaged.

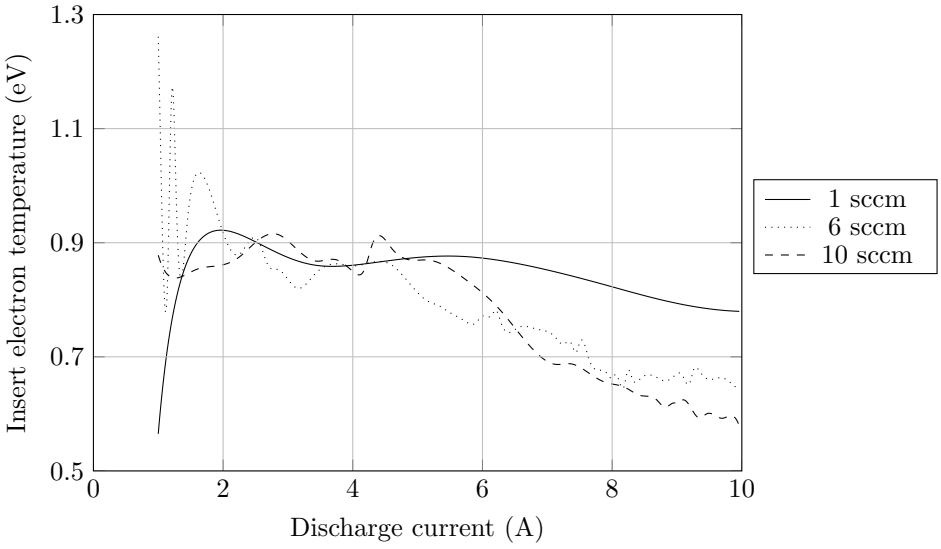

Figure 7. Insert electron temperature as calculated from Equations 17, 21 and 25, using electron density and temperature data from Ref. 25.

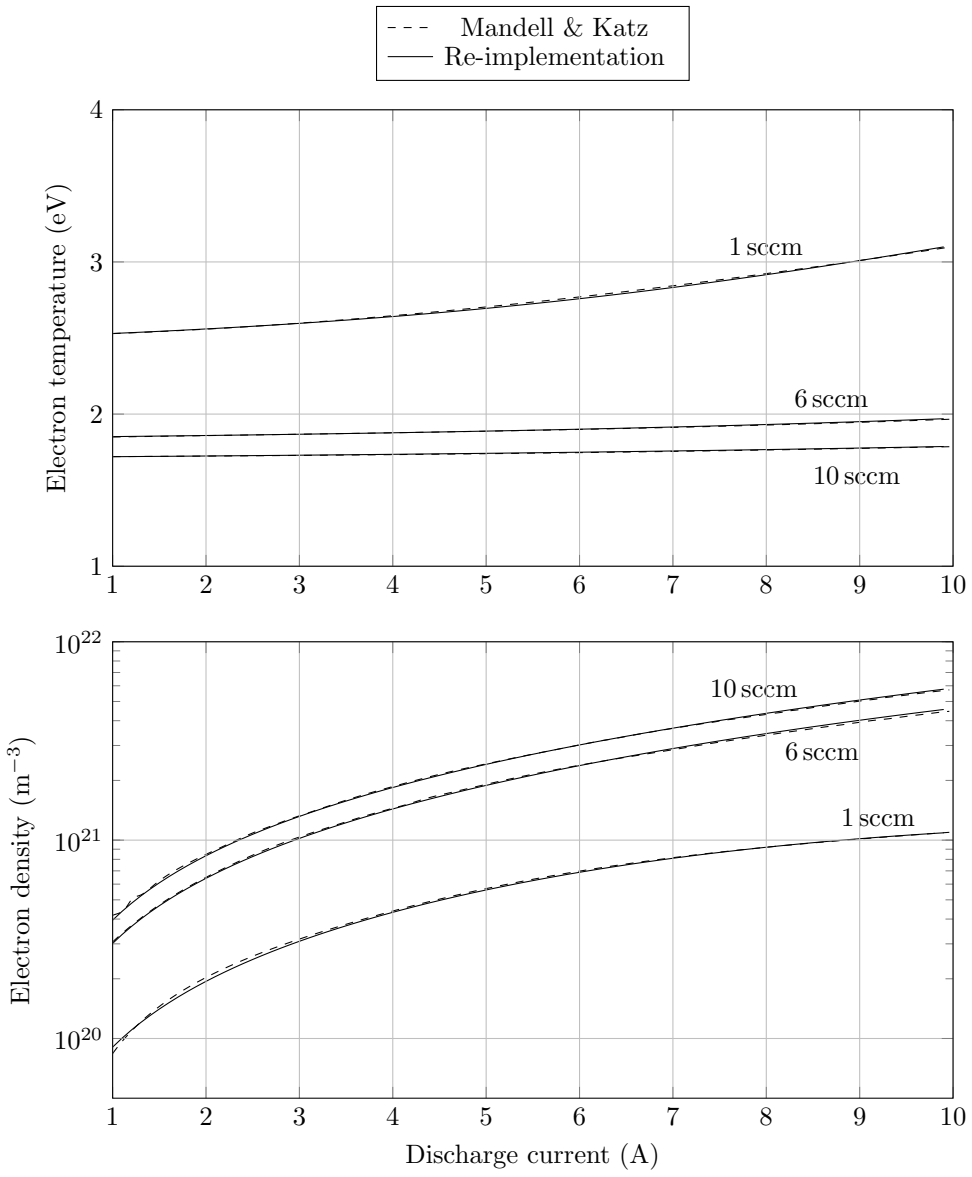

Figure 8. Comparison of Ref. 25 implementation to our re-implementation, for three mass flow rates (1, 3, and 6 sccm)

D. Capacci *et al.*[32]

Capacci *et al.* propose a complete model of a hollow cathode, consisting of an independent insert model, a simple orifice model, and a plume model. The plume is considered to extend from the cathode tip to the keeper plate. The goal of the model is to predict the performance of new hollow cathode designs by calculating the current-voltage characteristic of a cathode along with the cathode temperature.

1. Insert

The insert model is solved for the plasma and gas densities, the wall temperature, the plasma potential, and the electron temperature. It follows the latest revision of Siegfried and Wilbur outlined in Ref. 10, with an additional equation required to close the system. Capacci *et al.* suggest the addition of a two-temperature Saha equation (Equation 2), or an ion conservation equation (Equation 21). Additional modifications are introduced in the determination of the pressure in the insert region, evaluation of the emission length, and estimation of the heat loss in the insert surface power balance.

Neutral flow Much like Siegfried and Wilbur, Capacci *et al.* use an empirical relationship for the pressure in the insert region,

$$P = \frac{\dot{m}}{4r_o^2}\left(c_1 + c_2 I_d + c_3 I_d^2\right), \tag{33}$$

where c_1, c_2, and c_3 are empirical constants. The expression differs from Equation 4 with the addition of a quadratic dependency on the current. We were not able to compare the two empirical relationships, as the empirical constants are not specified in Ref. 32.

Emission length The emission length is defined without a thorough analysis of the collision processes present in the insert region. It is posited that the emission length is directly proportional to the insert radius, and is given by:

$$L_{\text{emit}} = c_4 r_c, \tag{34}$$

where c_4 is another empirical constant. The authors indicate that c_4 should take into account the non-uniformity of the thermionic process — suggesting this term should be evaluated with a separate model or experimental data. Capacci *et al.* set c_4 to a value of 0.5 in their study. This approach does not take into account any of the processes that influence the emission length. For example, higher mass flow rates and discharge currents typically reduce the emission length.

Heat loss The authors estimate the heat loss $\dot{q}_{th}$ from a separate thermal analysis of the insert region:

$$\dot{q}_{th} = 2r_c\left(c_5 + c_6 T_c\right) L_{\text{emit}}^{0.2}, \tag{35}$$

where c_5 and c_6 vary based on cathode geometry.

The remaining insert model equations are identical to those of Siegfried and Wilbur's refined model.

2. Orifice

The orifice model serves as a bridge between the insert and keeper regions. It is also used to estimate the voltage drop across the orifice. No plasma processes (e.g., ionization) are considered. Only electron-ion collisions are implemented in the finite plasma resistance, in effect considering the plasma to be fully ionized. While the approximation $\nu_{ei} \gg \nu_{en}$ may be true at low electron temperatures for sufficient ionization fractions (less than 1 eV and 1%) or for high ionization fractions (greater than 10%), the electron-neutral collisions can not be neglected for a typical cathode orifice operational point ($T_{eV} \approx 1 - 3\,\text{eV}$, $\alpha \approx 1 - 10\%$) as shown on Figure 9 for xenon.

The temperature of the electrons in the orifice is a free parameter, and is assumed to be equal to 1 eV in the calculations of Capacci *et al.*. The electron density is obtained by considering that the current is entirely carried by the electrons, with the fluid velocity of the electrons assumed to be equal to their thermal velocity

$$I_d = e n_e^{\text{orifice}} \left(\frac{e T_{eV}}{2\pi m}\right)^{1/2} \pi r_o^2. \tag{36}$$

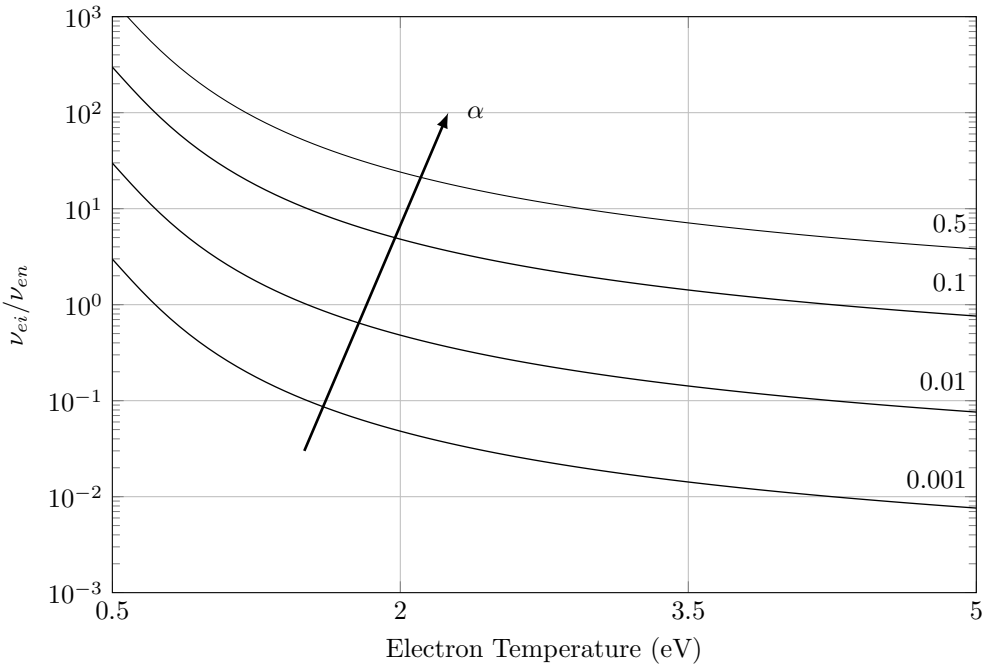

Figure 9. Ratio of electron-ion to electron-neutral collision frequencies, for increasing ionization fraction $\alpha = n_e/n_g$. The Coulomb logarithm is assumed to be equal to 7.1 — the average value for electron temperatures between 0.1 to 10 eV, and electron densities between 10^{18} and 10^{22} m^{-3}.

This assumption ignores the ions entrained outside of the orifice, and overestimates the fluid velocity of the electrons. For a given cathode, with only electrons carrying current, the fluid (or drift) velocity may be obtained as

$$u_e = \frac{I_d}{n_e e \pi r_o^2}. \tag{37}$$

For the NSTAR neutralizer cathode ($r_o = 0.14$ mm), 2-D simulations[33] have shown a maximum orifice plasma density of 2.2×10^{22} m^{-3}, and an electron temperature of 2.2 eV for a mass flow rate of 3.6 sccm and discharge current of 3.26 A. This amounts to an electron fluid velocity of $1.5 \cdot 10^4$ m/s, while the electron thermal velocity is equal to $6.2 \cdot 10^5$ m/s. Capacci *et al.* clearly overestimate the fluid velocity of the electrons, and, as a consequence, underestimate the plasma density in the orifice.

Neutral flow The orifice neutral density is estimated by assuming adiabatic and isentropic flow conditions:

$$n_g^{\text{orifice}} = n_g \left(\frac{\gamma + 1}{2} \right)^{-1/(\gamma-1)}. \tag{38}$$

Double sheath The authors assume the existence of a planar double sheath at the entrance of the orifice, though they ignore any ion contribution from the orifice in their insert model. A rigorous derivation of the double-sheath potential in the space-charge limited case over a distance d is described in Ref. 34 by Langmuir. Langmuir's result can be rewritten as[35]

$$\phi_{ds} = \left(\frac{9}{4} \frac{(J_e + J_i) d^2}{\epsilon_0 C_0} \sqrt{\frac{m}{2e}} \left(1 + \sqrt{\frac{m}{M}} \right)^{-1} \right)^{2/3}. \tag{39}$$

Capacci *et al.* consider the distance between the two planar sources of charged species to be the Debye length, and introduce the approximations $m/M \ll 1$, $C_0 \approx 7.5/4$, and $J_e + J_i \approx I_d/\pi r_o^2$. By conservation of current, the latter assumption amounts to ignoring ion and electron currents to the orifice wall. The double sheath

potential can now be computed in terms of electron temperature, density, and total discharge current:

$$\phi_{ds} = \left(\frac{9 I_d T_{eV}}{7.5 \pi r_o^2 n_e e} \sqrt{\frac{m}{2e}} \right)^{2/3}. \tag{40}$$

Ohmic heating An additional voltage contribution across the orifice comes from the plasma resistance:

$$V_\Omega = I_d R_{or}. \tag{41}$$

Capacci *et al.*'s expression for the plasma conductivity artificially inflates the contribution of the orifice to the total voltage drop from anode to cathode. The scaling constant is off by multiple orders of magnitude.

The assumptions of adiabatic and isentropic flow are also contradicted by introducing Ohmic contributions in the orifice region — the power deposited by Joule heating will clearly heat the neutral gas before it expands in vacuum. The existence of a double-sheath at the entrance of the orifice region is also disputed.

3. Keeper

Spherical double sheath Capacci *et al.* consider the existence of an additional double-sheath in the plume region, which has been observed by Siegfried and Wilbur in the keeper region in the plume mode.[20] The authors assume that the double-sheath is located at the tip of the cathode. This assumption implies the existence of ions streaming towards the orifice region, which have been ignored in both the orifice and insert models. The authors use a spherical model to estimate the current through the double-sheath as described in Ref. 36, which assumes a space-charge-limited process. Assuming that $I_d \approx I_e$, the ion current and double sheath voltage are:

$$I_i^{\text{tip}} = \alpha\left(r_o/r_{ds}^{\text{tip}}\right) I_d \sqrt{\frac{m}{M}}, \tag{42}$$

$$\phi_{ds}^{\text{tip}} = \left(\frac{I_i^{\text{tip}}}{4\pi\epsilon_0 j_0\left(r_o/r_{ds}^{\text{tip}}\right)} \sqrt{\frac{M}{2e}} \right)^{2/3}. \tag{43}$$

Both $\alpha\left(r_o/r_{ds}^{\text{tip}}\right)$ and $j_0\left(r_o/r_{ds}^{\text{tip}}\right)$ are tabulated as functions of r_o/r_{ds}^{tip} in Ref. 36.

The authors propose to calculate the external double sheath radius at the cathode tip by assuming that the Bohm criterion applies to the ions. This is in direct contradiction with the assumption of Wei and Wilbur, where the ions are considered to be cold at the sheath entrance. The proposed surface area over which the ions flow is incorrectly assumed to be a circle. To be consistent with the assumption of a hemispherical double sheath, it should be the area of a sphere, of radius r_{ds}^{tip}. The ion current is given by:

$$I_i^{\text{tip}} = e n_e^{\text{tip}} 2\pi \left(r_{ds}^{\text{tip}}\right)^2 \sqrt{\frac{e T_{eV}^{\text{tip}}}{M}}. \tag{44}$$

Neutral flow The neutral gas density, electron density, and temperature in this region are estimated assuming a spherical expansion and a simple two-temperature Saha equation model (see Equation 2), respectively. The resulting expression for the neutral density in the plume is:

$$n_g^{\text{tip}} = n_g^{\text{orifice}} \left(\frac{\psi r_o / \sin\psi}{(r_o/\sin\psi + L_{ck}/2)\psi} \right)^2 \tag{45}$$

This approach is similar to Siegfried and Wilbur's first attempt at hollow cathode modeling (Ref. 20), with the choked flow (Equation 1) being replaced by Equation 45.

4. Evaluation

Algorithm The insert, orifice, and keeper region models are solved for the electron and neutral gas densities in their respective regions. The insert model is entirely independent of the orifice and keeper regions. It outputs the electron and neutral gas densities, the plasma potential, wall temperature, and electron

temperature. In the orifice region, the plasma density is obtained from Equation 36, while the electron temperature is a free parameter. In the keeper region, these quantities are solved for using Equations 2, 44, and 45.

The total potential difference for the cathode is then estimated by summing each contribution from the different regions:

$$V_d = \phi_p + V_\Omega + V_{ds}^{\text{orifice}} + V_{ds}^{\text{tip}}. \tag{46}$$

Application The authors apply their solver to three cathodes — NCC A300, A5000, and A10000. Results of Capacci's implementation for the aforementioned cathodes are shown in Fig. 10. The model seems to be insensitive to changes in the mass flow rate, and is not able to reproduce the discharge characteristic of the cathode. The overall shape of the characteristic seems qualitatively correct, but the model under predicts the discharge voltage by 8 to 45%, even though the orifice plasma resistivity is overestimated.

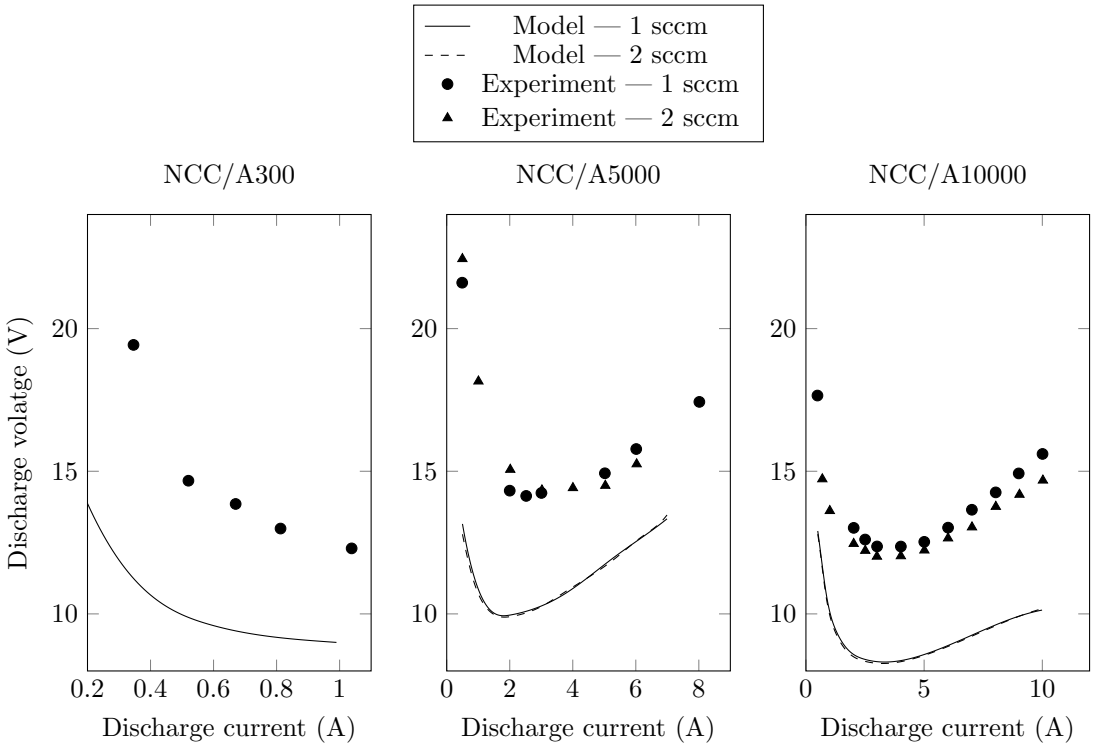

Figure 10. Comparison of the discharge characteristic for three different cathodes (A300, A5000, and A10000) using Capacci *et al.*'s hollow cathode model and experimental data from Ref. 32. No error bars were reported.

The results for the A300 cathode suggest that the majority of the discharge voltage comes from the plasma potential drop, as shown in Fig. 11. The electron temperature obtained in the insert region is also quite low — around 0.7 eV. The authors do note that the wall temperature is very sensitive to the effective work function. The introduction of a simple constant value for the calculation of the effective length also decreases the accuracy of the wall temperature prediction.

We were not able to reproduce results from this model, as the necessary information to solve for the different cathodes of interest — constants c_1 through c_6, as well as the gas plume expansion angle ψ — is not presented in Ref. 32. The specific contributions of the orifice and keeper models are not discussed, and no comparison with previous models is offered. The approach is promising and reuses key elements of Siegfried and Wilbur's successful low-current approach, but some assumptions are questionable, and the spherical double-sheath model is not implemented correctly. The plasma resistivity is also overestimated in the orifice region, and the model relies on experimental data (e.g. empirical pressure relationship). These factors combined render the approach unreliable in its current form.

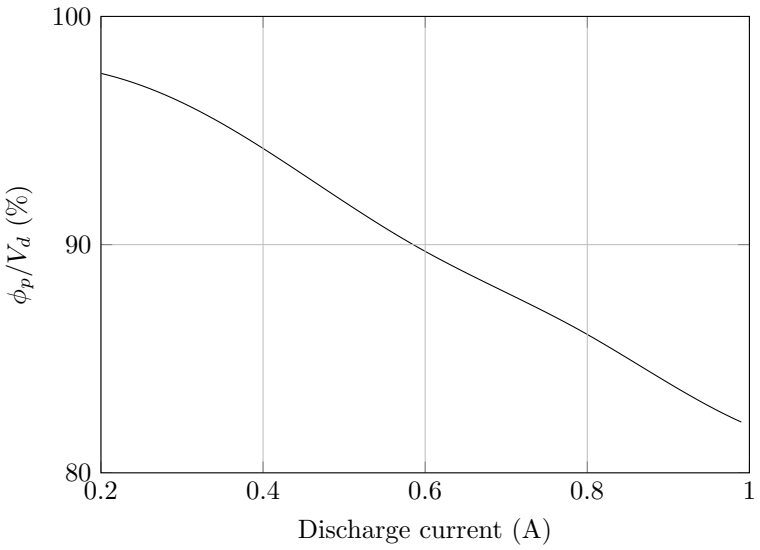

Figure 11. Ratio of predicted plasma potential to predicted discharge voltage from Ref. 32. The simulated cathode is the A300, for 1 sccm of xenon.

E. Domonkos[13,24]

Domonkos models cathode performance by considering the orifice and the insert regions separately. The model for the orifice region is based on that of Mandell and Katz[13,25] (with the addition of a current balance equation) and requires the orifice wall temperature, mass flow rate, and discharge current as input. The full model is comprised by current, ion, and energy conservation equations in each volume. The insert and orifice region models are coupled through the electron/ion exchange in the orifice entrance and the insert electron temperature (via its contribution to the electron convection balance in the orifice). Each of the coupled models has its own set of free parameters needed to approximate the excitation and ionization processes taking place and to describe the electron emission and power deposition in the insert. Unfortunately, Domonokos's model description contains typographical or physical errors in many of the equations (repeated in all references for the model, and in later models citing his work[14,37]), making it difficult to implement without ambiguity. We have attempted to correct typographical errors in the equations that follow, pointing out inconsistencies in the physical treatment when they appear.

1. Orifice model

The orifice model uses ion conservation, current continuity, and conservation of energy in the plasma volume to solve for the plasma density and electron temperature in the orifice. In order to evaluate the neutral density, the gas flow through the orifice is assumed to occur at the sonic velocity characteristic of the orifice wall temperature.

Ion conservation The ion balance in the orifice region equates the creation of ions through electron-impact ionization and the influx of ions from the insert region to the outflux of ions through the orifice inlet and outlet and ion losses to the walls of the orifice, and is given by:

$$\left(\frac{dN_i}{dt}\right)_{\text{iz}} + \underbrace{\left(\frac{dN_i}{dt}\right)_{\text{in}}}_{\text{neglected}} - \left(\frac{dN_i}{dt}\right)_{\text{out}} = 0. \tag{47}$$

The second term in Equation 47 is neglected due to the assumption that a double sheath exists at the constriction of the orifice entrance, preventing the flow of ions from the insert region. The ionization rate coefficient is calculated by integrating the product of the velocity-dependent ionization cross-section and the electron velocity over a Maxwellian EEDF. Domonkos considers only direct electron-impact ionization and

neglects step-wise ionization in the orifice:

$$\left(\frac{dN_i}{dt}\right)_{\text{iz}} = \left(\pi r_o^2 L_o\right)\left(\frac{m}{2\pi e T_{eV}}\right)^{3/2} 4\pi n_e n_g \int_0^{+\infty} v^3 \sigma_{iz}(v) \exp\left(-\frac{mv^2}{2eT_{eV}}\right) dv. \tag{48}$$

The ions leaving the volume exit through either the sheath surrounding the orifice surfaces (assumed to include the orifice inlet) or through thermal efflux at the orifice outlet, towards the keeper and anode. The Bohm condition is used to calculate the flux of ions towards the wall and through the double sheath:

$$\left(\frac{dN_i}{dt}\right)_{\text{out}} = \underbrace{0.61 n_e \sqrt{\frac{eT_{eV}}{M}}\left(2\pi r_o L_o + \pi r_o^2\right)}_{\text{sheaths}} + \underbrace{\frac{1}{4} n_e \sqrt{\frac{8eT_{iV}}{\pi M}} \pi r_o^2}_{\text{thermal}}. \tag{49}$$

Using the Bohm criterion to calculate the ion flux to the orifice surfaces is justifiable, due to the assumption that the orifice walls are not emitting. Therefore the ion acceleration in the pre-sheath should be unmodified.[15] However, applying the Bohm criterion to the double sheath is questionable. The electrons and ions are counterstreaming in the case of the double sheath, rather than traveling in the same direction, as in the case of the wall sheath, and the ion current should instead be solved for in a manner consistent with the double sheath model used (e.g., using the Langmuir ratio $\sqrt{m/M}$ to find the ratio of ion to electron currents[34]).

Mass conservation The neutral gas density in the orifice is calculated using mass conservation, assuming sonic flow:

$$n_g = \frac{\dot{m}}{M \pi r_o^2 \sqrt{\gamma R T_g}}. \tag{50}$$

The (static) neutral gas temperature is assumed to be equal to the orifice plate temperature, which must be obtained from experimental data. In using this equation for the *neutral* density, Domonkos implicitly assumes that 100% of the neutral gas input exits the cathode in the same state, disregarding ionization processes and the electron pressure contribution. Domonkos seems to imply at various points within the coupled models that n_g instead refers to the density of *heavy* particles — both ions and neutrals — which is more reasonable from a mass conservation standpoint. However, he then uses this value as the neutral density for the purposes of calculating the ionization rate, reducing it by the plasma (ion) density when calculating the excitation rate. The target species in both cases should have the same density, unless excited ions or multiple ionizations are considered.

In addition, it is unclear whether the appropriate velocity for the ions leaving the volume through the orifice outlet is that of the fluid (which would be required for continuity if the density calculated above is the *heavy* particle density) or the ion thermal velocity. The difference between these values is relatively small, however, given that the ratio of the neutral sound speed to the ion thermal velocity is $\sqrt{\frac{5\pi}{24}} \approx 0.81$ for a monatomic propellant. Domonkos uses the ion thermal velocity to calculate the ion flux through the orifice outlet, but the overall contribution from the exiting ion current is small regardless of the flow velocity used.

Current continuity Current continuity in the orifice region is used to find the electron current entering the orifice from the insert region plasma. A simplified picture of the orifice currents is shown in Fig. 12. Ions leave the orifice at the thermal velocity through the outlet (I_i^{emit}), at the Bohm velocity through the double sheath (I_i^{ds}) at the orifice inlet, or recombine at the orifice walls (I_i^{walls}), having been accelerated to the Bohm velocity by the orifice wall sheath. No ion current flows from the insert region into the orifice due to the double sheath.

The total discharge current can be calculated at the downstream end of the orifice as the difference between the electron and ion currents leaving the orifice:

$$I_d = I_e^{\text{orifice}} - I_i^{\text{emit}}, \tag{51}$$

which, along with the ion flux terms in the orifice, can be used to calculate the electron current from the insert. Domonkos gives the following expression for the insert electron current:

$$I_d = I_e^{\text{insert}} + I_i^{\text{wall}} + I_i^{\text{ds}} - I_i^{\text{emit}} \tag{52}$$

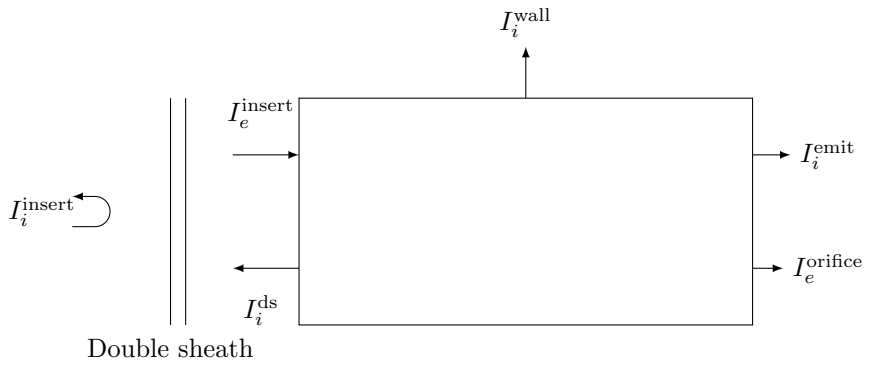

Figure 12. 0-D cell representation of the orifice currents.

Domonkos's proposed relationship at the downstream end of the orifice features an unnecessary term, I_i^{emit}, and consequently violates conservation of charge; since no electrons are lost in the orifice, the electron current at the outlet should be equal to the sum of the electron current at the inlet and the electron current generated by ionization in the orifice volume:

$$I_e^{\text{orifice}} = I_e^{\text{insert}} + I_e^{\text{created}} \tag{53}$$

Because electrons and ions are created in pairs, and all ions created in the orifice must also leave the orifice (for steady-state conditions), we can express the electron current due to volume ionization in terms of the ion outfluxes:

$$I_e^{\text{created}} = I_i^{\text{wall}} + I_i^{\text{ds}} + I_i^{\text{emit}} \tag{54}$$

Equations 51, 53, and 54 can be combined to yield the correct relationship:

$$I_d = I_e^{\text{insert}} + I_i^{\text{wall}} + I_i^{\text{ds}} \tag{55}$$

I_i^{wall}, I_i^{ds}, and I_i^{emit} are obtained as shown in Equation 49, expressed separately below:

$$I_i^{\text{wall}} = 0.61 n_e e \sqrt{\frac{eT_{eV}}{M}} \left(2\pi r_o L_o\right) \tag{56}$$

$$I_i^{\text{ds}} = 0.61 n_e e \sqrt{\frac{eT_{eV}}{M}} \left(\pi r_o^2\right) \tag{57}$$

$$I_i^{\text{emit}} = n_e e \frac{1}{4} \sqrt{\frac{8eT_{iV}}{\pi M}} \pi r_o^2 \tag{58}$$

In Domonkos's approach, the two current continuity Equations 51 and 55 yield both the electron current coming from the insert, I_e^{insert}, and the electron current leaving the orifice, I_e^{orifice}. Because the discharge current increases along the length of the orifice, their determination is necessary for the calculation of the Ohmic losses in the orifice. We note that either I_e^{insert} or I_i^{ds} is not actually an unknown, as these quantities are tied together through the double sheath relationship,[34]

$$I_e^{\text{insert}} = I_i^{ds} \sqrt{\frac{M}{m}}. \tag{59}$$

The double sheath ion current, I_i^{ds}, has been assumed to be known and set equal to the Bohm current in Domonkos's approach, which likely over-predicts the required electron current, I_e^{insert}, and therefore the double sheath voltage if calculated in a self-consistent manner.

Energy conservation Power deposition in the orifice volume is assumed to take place via Ohmic heating, balanced by losses due to ionization, excitation, and electron convection:

$$\dot{q}_\Omega = \dot{q}_{iz} + \dot{q}_{ex} + \dot{q}_{\text{conv}}. \tag{60}$$

Domonkos assumes that the electron current increases linearly along the orifice length due to the previously discussed ionization taking place in the orifice using the following expression,

$$I_e(x) = I_e^{\text{insert}} + bx, \tag{61}$$

where $b = \frac{I_e^{\text{orifice}} - I_e^{\text{insert}}}{L_o}$. This assumption implies that the electron density increases along the length of the orifice if the drift velocity is constant (no electron losses are considered in the orifice); while this is inconsistent with the 0-D approach, it does make sense to attempt to account for the increase in electron current across the orifice (volume ionization within the entire cathode has been estimated to account for up to 30% of the total discharge current[10]). The Ohmic heating term is calculated using the mean-square electron current over the length of the orifice:

$$\dot{q}_\Omega = R_{or} \left\langle I_e(x)^2 \right\rangle = \eta_p \frac{L_o}{\pi r_o^2} \left(\left(I_e^{\text{insert}}\right)^2 + I_e^{\text{insert}} b L_o + \frac{1}{3} b^2 L_o^2 \right) \tag{62}$$

Even if the electron current were to increase by 50% along the orifice length, however, the difference in Ohmic power deposition obtained using the mean-square current versus simply using the outlet electron current is only about 8%, assuming constant resistivity.

The orifice plasma resistivity is calculated using Equation 28, with the electron-ion collision frequency from the NRL plasma formulary,[38]

$$\nu_{ei} = 3.9 \times 10^{-12} \frac{n_e}{T_{eV}^{3/2}} \ln \Lambda. \tag{63}$$

The electron-neutral collision frequency is evaluated using a calculated reaction rate based on experimental cross-section data and a Maxwellian EEDF divided by the plasma density. The Coulomb logarithm differs slightly from Mandell and Katz's definition given earlier:

$$\ln \Lambda = 23 - \frac{1}{2} \ln \left(\frac{10^{-6} n_e}{T_{eV}} \right). \tag{64}$$

The ionization losses are calculated by multiplying the ionization rate in the volume by the ionization energy:

$$\dot{q}_{iz} = e\epsilon_i \left(\frac{dN_i}{dt} \right)_{\text{iz}}. \tag{65}$$

The excitation losses are found in a similar manner:

$$\dot{q}_{ex} = e\epsilon_{ex} \left(\frac{dN_{ex}}{dt} \right). \tag{66}$$

The excitation rate, $\left(\frac{dN_{ex}}{dt}\right)$, is obtained by integrating over the total excitation cross-section:

$$\left(\frac{dN_{ex}}{dt} \right) = \left(\pi r_o^2 L_o\right) \left(\frac{m}{2\pi e T_{eV}} \right)^{3/2} 4\pi n_e n_g \int_0^{+\infty} v^3 \sigma_{ex}(v) \exp\left(-\frac{m v^2}{2 e T_{eV}} \right) dv. \tag{67}$$

In order to calculate the power loss due to excitation, the excited states are lumped with the average excitation energy, ϵ_{ex}, as a free parameter in the model. Its value is set at 10 eV, though a more rigorous model would consider the different excitation levels in the gas of interest, and compute the average excitation energy. Doing so would require knowledge of the densities of each excited state in order to evaluate the contribution of stepwise excitations, which could be found using a Collisional-Radiative model similar to that implemented by Peters and Wilbur[39] for mercury.

Finally, convection losses are given by the difference between the power carried out of the orifice by the outgoing electron current and the power input from the insert electron current. Following Mandell and Katz, Domonkos neglects the factor of 5/2 that should be present in each of the convection terms:

$$\dot{q}_{\text{conv}} = \left(I_e T_{eV}\right)_{\text{orifice}} - \left(I_e T_{eV}\right)_{\text{insert}}. \tag{68}$$

ALGORITHM By first calculating the neutral (or heavy) density, n_g, using the sonic flow condition, the remaining orifice model equations can be solved for the orifice electron temperature and plasma density. Domonkos notes that while the insert electron temperature is an input to the orifice model, and can be obtained through the coupled insert model, an average value may also be used due to the small variation in insert electron temperature for most operating conditions (though this may be due to the very high pressures used for Domonkos's particular cathode geometry). If the density calculated from the sonic condition at the orifice is assumed to be the neutral density, or the reduction of the heavy density by the plasma density is neglected in the ionization rate calculation, then the ion continuity equation is a function of only the neutral/heavy density and the electron temperature, the former being fixed by the flow model. This computational expedience may be the reason that Domonkos does not use the same target species density for excitation and ionization rate calculations. Either of these simplifications would be reasonable only for low ionization fractions. The plasma density can then finally be obtained from the energy equation. If these equations are not solved simultaneously, an iterative procedure may be necessary to ensure convergence.

2. Insert model

Similar balance equations are used to model the insert region: ion conservation, current continuity, and energy conservation are considered along with a pressure calculation using a form of Poiseuille flow modified to account for the pressure drop encountered at the sudden flow constriction of the orifice.

POISEUILLE FLOW MODEL In order to calculate the pressure in the insert region, the pressure drop along the orifice length is estimated using Poiseuille flow and the aforementioned correction due to the flow constriction,

$$P_{\text{insert}} = \sqrt{\dot{m}\frac{16\mu}{\pi r_o^4} R T_o L_o + P_{\text{sonic}}^2} + \frac{1}{2}\bar{\rho}\bar{u}^2\left(1 + K_L\right), \tag{69}$$

where P_{sonic} is the pressure calculated in the orifice model for the assumed choked-sonic flow through the orifice, $\bar{\rho}$ is the average density, $\bar{u}$ is the average flow velocity, and K_L is the loss coefficient due to the constriction (≈ 0.5). The average density is evaluated at the arithmetic average of the pressures at each end of the orifice, using the upstream pressure without the correction as P_{insert}. The average velocity can be found using the linearized pressure gradient along the length of the orifice:

$$\bar{u} = \frac{r_o^2}{8\mu}\left(\frac{P_{\text{insert}} - P_{\text{sonic}}}{L_o}\right). \tag{70}$$

This flow model predicted reasonable, but low, values of the pressure in Domonkos's experimental cathodes. This may be due to the pressure contribution from the discharge, or heating of the neutral gas by charge exchange.[40] A brief derivation of this model is given in Appendix C of Ref. 13.

ION CONSERVATION Domonkos considers ionization due to both primary (thermionically emitted) and plasma (thermalized/Maxwellian) electrons, the former through the creation of excited states which are then ionized by the latter. The primary electrons are emitted with a Maxwellian distribution at the emitter temperature, "shifted" to account for the acceleration of electrons by the sheath potential. The sheath potential is assumed to be equal to the plasma potential in this model. The distribution function used is given by:

$$f_b(v_e) = 4\pi\left(\frac{m}{2\pi e T_{eV}}\right)^{3/2} v_e^2 \exp\left(-\frac{m\left(v_e - v_b\right)^2}{2eT_{eV}}\right). \tag{71}$$

The proposed distribution is incorrect as the shift is applied directly to the speed distribution, as opposed to the velocity in the direction of beam propagation. The distribution given in Equation 71 is also not properly normalized. A more accurate representation of the beam distribution would be given by:

$$f_b(\mathbf{v}) = 2\left(\frac{m}{2\pi e T_{eV}}\right)^{3/2} \exp\left\{-\frac{m\left[v_x^2 + v_y^2 + \left(v_z - v_b\right)^2\right]}{2eT_{eV}}\right\}\theta(v_z - v_b). \tag{72}$$

In Equation 72, the velocity distribution is shifted only in the direction of the electron beam acceleration (taken to be the z-direction), and the Heaviside θ makes the distribution one-sided, as no particles should have a z-direction velocity less than that of the beam no particle can have a negative z-velocity at the wall or else it would not leave the emitter. This equation is slightly more difficult to integrate than the original distribution, but it can be put into a form more appropriate for integration by introducing $v_\perp = \sqrt{v_x^2 + v_y^2}$ and $|v| = \sqrt{v_\perp^2 + v_z^2}$:

$$\iiint f_b(\mathbf{v})\, d^3v = 4\pi \left(\frac{m}{2\pi e T_{eV}}\right)^{3/2} \int_{v_b}^{+\infty} \int_0^{+\infty} v_\perp \exp\left\{-\frac{m\left[v_\perp^2 + (v_z - v_b)^2\right]}{2eT_{eV}}\right\} dv_\perp\, dv_z. \tag{73}$$

The corresponding reaction rate coefficient would therefore be given by:

$$\langle \sigma v \rangle = 4\pi \left(\frac{m}{2\pi e T_{eV}}\right)^{3/2} \int_{v_b}^{+\infty} \int_0^{+\infty} |v| \sigma(|v|) v_\perp \exp\left\{-\frac{m\left[v_\perp^2 + (v_z - v_b)^2\right]}{2eT_{eV}}\right\} dv_\perp\, dv_z. \tag{74}$$

Given the large disparity between the beam velocity induced by the emitter sheath and the thermal velocity characteristic of the emitter temperature, there seems to be little reason to introduce such a distribution unless the beam energy is close to the threshold energy for a process of interest. Typical sheath and plasma potentials for hollow cathodes are in the 3–12 V range, while emitter temperatures are 0.1–0.2 eV. Domonkos's choice of 8 V for the plasma potential (a free parameter in the model) is close to the first excitation energy of xenon, so the tail of the beam distribution may contribute to excitation, but the arbitrary nature of this plasma potential value makes it difficult to assess whether the finite beam temperature is important for a real cathode. The relatively low energy required (3.4 eV)[41] for ionization from xenon metastable states would make these events far more likely to contribute to stepwise ionization if a sufficient density of metastables exists within the mean free path of the beam electrons. The energy the electrons typically gain from the sheath potential being less than the threshold for direct ionization (at least in the case of xenon), Domonkos's approach of comparing the ionization and excitation mean free paths is likely unnecessary.

Domonkos modifies Equation 48 to account for multi-step ionization, which is assumed to occur in the region outlined in Figure 14. The mean free path for excitation λ_{ex} is, by definition:

$$\lambda_{ex} = \frac{1}{n_g \sigma_{ex}}. \tag{75}$$

In order to account for the effect of the finite-temperature beam of primary electrons, Domonkos uses the following expression:

$$\lambda_{ex} = \frac{\langle v \rangle_{beam}}{n_g \langle \sigma_{ex} v \rangle_{beam}}. \tag{76}$$

This expression removes the effect of the normalization problems mentioned earlier. Even without the normalization issues, however, Domonkos's use of the distribution given by Equation 71 introduces significant error (approximately 40% at $\phi_p = 8$ V) in the effective cross-section for excitation over most of the energy range of interest, as shown in Figure 13. The results shown were found by performing the integral in Equation 74 over all excitation cross-sections in the LXCAT Hayashi database.[30]

An arbitrary, fixed percentage of the primary excitation events, p_{ex}, is assumed to create ions through multi-step ionization. This percentage is a free parameter and attempts to account for the ions generated by stepwise ionization of beam-excited neutrals. The total ionization rate in the insert volume is given by:

$$\left(\frac{dN_i}{dt}\right)_{\text{iz}} = \pi r_c^2 L_{\text{emit}} n_e n_g \langle \sigma_{iz} v_e \rangle_{\text{plasma}} + p_{ex} \pi L_{\text{emit}} \left(r_c^2 - (r_c - 2\lambda_{ex})^2\right) n_e^{\text{primary}} n_g \langle \sigma_{ex} v_e \rangle_{\text{primary}}. \tag{77}$$

The density of primary electrons, n_e^{primary}, is the density of emitted electrons as they enter the bulk plasma, with a velocity, v_d, determined by the plasma potential. The subscripts "plasma" and "primary" in Equation 77 for the rate coefficients indicate that those quantities are to be determined using

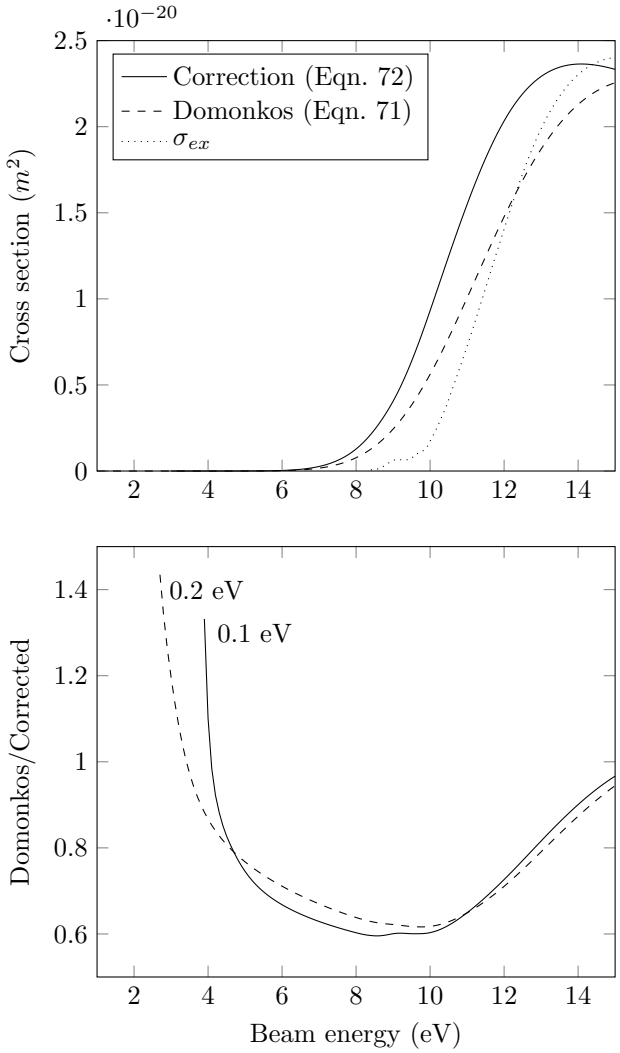

Figure 13. Comparison of the distribution-averaged collision cross-sections. Top: Beam-distribution-averaged excitation cross-section computed with Equation 71 (dashed line), and Equation 72 (solid line). The excitation cross-section for a monoenergetic beam is shown with a dotted line. Bottom: Ratio of the distribution-averaged excitation cross-sections computed using the two approaches for two beam electron temperatures.

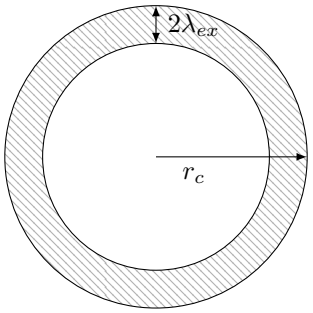

Figure 14. Region of multi-step ionization.

the distribution-averaging appropriate for either the Maxwellian plasma electrons or the beam electrons, respectively. Domonkos uses the thermionic current density to calculate the density of primary electrons,

$$n_e^{\text{primary}} = \frac{J_{em}}{ev_d}, \tag{78}$$

where the velocity of electrons is obtained through energy conservation of ballistic electrons,

$$v_d = \left(\frac{2e\phi_p}{m}\right)^{1/2}, \tag{79}$$

and J_{em} is calculated in the same manner as for Siegfried and Wilbur's model, but the Richardson constant is set equal to 60 $A/(cm^2K^2)$. The effective work function is evaluated using the expression for the electric field at the cathode surface from Prewett and Allen.[15] The emission length, L_{emit}, was introduced in Domonkos's equation for the ionization rate, and is set equal to the insert radius, r_c.

Current conservation The total discharge current is represented as the sum of the emitted electron current, the ion and electron fluxes collected on the cathode and orifice surfaces — including ions thermally diffusing upstream — and the ion flux towards the walls of the orifice. Domonkos gives the following relationship for the current continuity:

$$I_d = I_{em} + I_i^{\text{coll}} - I_e^{\text{coll}} - I_i^{\text{emit}}. \tag{80}$$

This expression, as for the case of the expression in the orifice, does not conserve charge. A correct approach considers either the insert control volume with an influx of ions from the double sheath, and outflux of electrons to the double sheath (see Fig. 15), or the combination of both orifice and insert control volumes. Using the former approach, the current balance yields:

$$\begin{aligned} &I_{em} - I_e^{\text{coll}} + I_i^{\text{coll}} + I_i^{th} = I_e^{\text{insert}} + I_i^{ds} \\ \Leftrightarrow\ &I_{em} - I_e^{\text{coll}} + I_i^{\text{coll}} + I_i^{th} = I_d - I_i^{\text{wall}} \\ \Leftrightarrow\ &I_d = I_{em} - I_e^{\text{coll}} + I_i^{\text{coll}} + I_i^{th} + I_i^{\text{wall}}. \end{aligned} \tag{81}$$

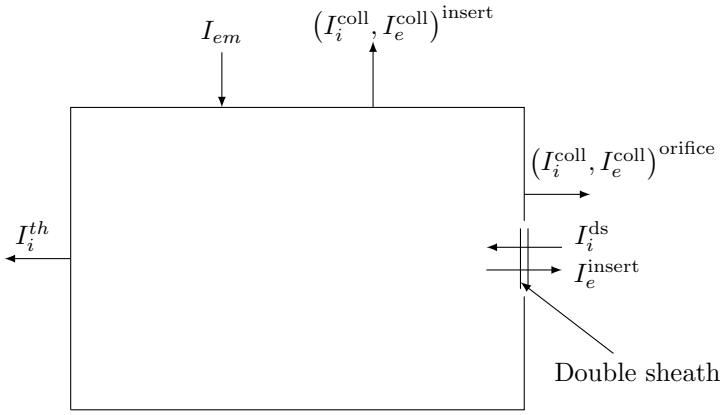

Figure 15. 0-D cell representation of the insert currents.

The ion current to the orifice wall, I_i^{wall} is used to distinguish the ion current collected on the internal orifice walls from that collected on the insert and orifice plate surfaces, I_i^{coll}.

The thermionic current density is given by Equation 8. As mentioned earlier, Domonkos considers the plasma potential to be a free parameter, restricted to the range of 8 to 12 V, based on experimental data. The current density from the ions collected by the cathode and orifice surfaces is obtained using Equation 6 modified for the existence of a pre-sheath (assuming that the potential drop is that required to accelerate the ions to the Bohm velocity, unmodified by the electron emission in the insert):

$$I_i^{\text{coll}} = \underbrace{0.61en_e\sqrt{\frac{eT_{eV}}{M}}2\pi r_c L_{\text{emit}}}_{\text{to inner cathode surface}} + \underbrace{0.61en_e\sqrt{\frac{eT_{eV}}{M}}\pi(r_c^2 - r_o^2)}_{\text{to orifice plate}}. \tag{82}$$

The current due to the backstreaming electrons is expressed in terms of the random electron current density as:

$$I_e^{\text{coll}} = J_r \left(2\pi r_c L_{\text{emit}} + \pi(r_c^2 - r_o^2)\right). \tag{83}$$

The random electron current density is given by:

$$J_r = \frac{1}{4}\left(\frac{8eT_{eV}}{\pi m}\right)^{1/2} n_e e \exp\left(-\frac{e\phi_p}{k_B T_{eV}}\right) \tag{84}$$

The thermal ion current diffusing upstream, I_i^{th}, is accounted for using the expression for I_i^{emit}, with the orifice radius replaced by the cathode inner radius.

Conservation of energy The insert plasma gains energy through Ohmic heating, ion flux from the orifice, and sheath-accelerated thermionic electrons. Losses are comprised by ionization, excitation of neutral particles, ion and electron convection, and electron backstreaming:

$$\dot{q}_\Omega + \dot{q}_{\text{ori}} + \dot{q}_{em} = \dot{q}_{iz} + \dot{q}_{ex} + \dot{q}_{\text{conv}} + \dot{q}_{\text{coll}}. \tag{85}$$

The boundaries of the control volume should be drawn carefully. We could include or exclude the pre-sheath in this approach. Domonkos chooses to ignore the pre-sheath potential, though includes its effect on the ion current due to the density decay. Domonkos considers that the electron current is the only driver for Ohmic heating. Ohmic heating is due to the net current, I_d, where we consider only electron-heavy collisions for resistivity. The resistivity is calculated in a similar fashion as in the previous section, though the author here assumes the current to be conducted radially. To account for radial conduction, Domonkos introduces an average cross-sectional area, but misses a factor of π shown in the corrected expression:

$$A_{\text{eff}} = \frac{\int_0^{r_c} (2\pi r L_{\text{emit}})\, r dr}{\int_0^{r_c} r dr} = \frac{4}{3}\pi r_c L_{\text{emit}}. \tag{86}$$

The corrected expression for the Ohmic heating is given by Equation 87:

$$\dot{q}_\Omega = I_d^2 \eta_p \frac{r_c}{(4/3)\,\pi r_c L_{\text{emit}}}. \tag{87}$$

Orifice ions carry both the average energy of (assumed) Maxwellian particles crossing a boundary surface and the potential energy obtained through the double-sheath assumed to exist at the entrance of the orifice,

$$\dot{q}_{\text{ori}} = I_i^{ds}(\phi_{ds} + 2T_{iV}), \tag{88}$$

where the expression is in term of the orifice quantities. The double-sheath potential is estimated with the same expression as Capacci *et al.* (Equation 40). Domonkos uses the total discharge current in Equation 40. This is incorrect, as the net current through the double-sheath is equal to $I_i^{ds} + I_e^{insert} \neq I_d$ (see Equation 55).

The thermionic electrons entering the volume carry the cathode fall voltage and a finite thermal energy due to the wall temperature. The characteristic energy of electrons leaving the wall is twice the wall temperature.[42] The cathode fall voltage is assumed to be equal to the plasma potential in Domonkos's approach. The thermal energy term should appear here with a factor of 2, as opposed to $\frac{3}{2}$; realistically, however, unless a very exotic emitter material were used, the emitter temperature is negligible compared to the sheath potential and the term can simply be left out. The corrected expression for the emitted electron power is:

$$\dot{q}_{em} = I_{em}\left(\phi_p + 2\frac{k_B T_c}{e}\right). \tag{89}$$

Generated ions contribute to ionization losses — this energy is lost from the plasma volume through the diffusion of ions upstream of the insert, and the collection of ions at the insert and orifice walls:

$$\dot{q}_{iz} = \left(I_i^{th} + I_i^{coll}\right)\epsilon_i \tag{90}$$

Both plasma and beam (also identified as "primary") electrons participate in energy loss through excitation. Domonkos provides a relationship which is dimensionally inconsistent; we have corrected the equation below:

$$\dot{q}_{ex} = e\epsilon_{ex}\left(n_e n_g \langle\sigma_{ex} v_e\rangle_{\text{plasma}} + n_e^{\text{primary}} n_g \langle\sigma_{ex} v_e\rangle_{\text{primary}}\right)\pi L_{\text{emit}} r_c^2 \tag{91}$$

Particles are collected at the insert and orifice walls, and the power they carry is given by:

$$\dot{q}_{\text{coll}} = \left(I_i^{th} + I_i^{\text{coll}}\right) 2T_{iV} + I_e^{\text{coll}}(\phi_p + 2T_{eV}). \tag{92}$$

Though it is important to note that while the pre-sheath potential has been neglected, the energy of the ions leaving the plasma volume at the pre-sheath edge ($T_{eV}/2$, without any modification for electron emission) is likely of the same order of magnitude or greater than $2T_{iV}$. Finally, electrons leave the volume through the double-sheath. Domonkos implicitly assumes that these electrons are the only charge carriers flowing through the sheath, and proposes that the convected current is equal to I_e^{insert} yielding the following expression for the convection power:

$$\dot{q}_{\text{conv}} = \frac{5}{2} I_e^{\text{insert}} T_{eV}. \tag{93}$$

3. Additional comments

The model requires the total discharge current, flow rate, cathode material, and cathode geometry as inputs. The four free parameters considered are p_{ex}, excitation energy in both orifice and insert regions, and the plasma potential in the insert region. Domonkos also mentions the work function as a free parameter in his model, though the values for most cathode materials are known and the parameter was constrained to a small range in his calculations. Domonkos compares his results for the AR6, AR3, and SSPC cathodes, and performs a sensitivity analysis of his model. The author shows that ϵ_{ex} and p_{ex} affect both the number density and power consumption significantly, with more than 30% variation of plasma density over a 5%-range for p_{ex}. Domonkos chooses the values of $\epsilon_{ex} = 5$ eV and $p_{ex} = 5\%$ in the insert region in order to account for the reduction in effective excitation energy due to stepwise processes; other authors choose a lumped value of 10 eV for the excitation energy of xenon as Domonkos uses in the orifice region.

Domonkos's model made an admirable attempt to be more comprehensive than other models, but in most cases the inclusion of complicating effects incurred the costs of increased sensitivity to free parameters and errors in implementation. Without more complete characterization of the stepwise processes in xenon-fed orificed hollow cathodes, it is difficult to evaluate the efficacy of Domonkos's attempts to simplify their contribution. We were not able to re-implement or confirm the results of the original model as described in Refs. 13 and 24. Domonkos gives intermediate calculations only for two different sets of operating conditions in the insert and orifice[13] and we could not find any combination of using his original equations or our own corrections that would reproduce these values, so it appears the original implementation details have been have been lost.

F. Goebel and Katz[11,43]

Goebel and Katz describe a 0-D model in their 2008 textbook[11] based on power balances for the insert plasma and the thermionic emitter, a current balance, and an ambipolar diffusion model (effectively an ion balance) for the electron temperature. A simplified power balance and the same ambipolar diffusion model are solved in the orifice in order to find the plasma density and electron temperature, respectively.

A Poiseuille flow model is used for the neutral gas pressure in both the orifice and insert, though the average pressure in each region is used for the model. The Poiseuille flow model used is identical to that of Domonkos (Equation 69), excluding the correction due to the orifice constriction and the use of the sonic condition for the orifice outlet pressure, which must be specified directly. The pressure found is assumed to be that of the *neutral* species.

Emission is assumed to be described by the Richardson-Dushman equation, with no modification due to the sheath electric field. By assuming no variation in the axial direction and charge-exchange-limited ambipolar diffusion, the electron temperature can be found solely as a function of neutral gas pressure, ignoring the effects of the plasma on the flow and assuming a constant temperature for the heavy species. The neutral temperature is usually taken to be 2–4 times the absolute wall temperature due to charge-exchange collisions between the ions and neutrals.[11,40]

1. Insert model

Goebel and Katz's insert model does not rely on inputs from the orifice model; once the neutral pressure has been calculated from the Poiseuille flow model, the electron temperature can be found as a function of only pressure and cathode radius.

Ambipolar Diffusion Unique to the approach of Goebel and Katz, modeling ion conservation using an ambipolar diffusion approach yields an estimate of the spatial variation in plasma density within the insert region as well as the electron temperature. Using the electron and ion momentum equations, neglecting the electron current and neutral drift terms, and assuming that ion diffusion is limited by resonant charge exchange (due to the relatively large cross section on the order of $1 \times 10^{-18}\text{m}^2$ for the inert gases[44,45]) the ambipolar diffusion coefficient can be found:

$$D = D_a = \frac{e}{M} \frac{T_{iV} + T_{eV}}{n_g \sigma_{\text{CEX}} v_{\text{scat}}}. \tag{94}$$

The neutral scattering velocity, v_{scat}, in Equation 94 is assumed to be the (1-D) ion thermal velocity. Goebel and Katz assume the ionization rate coefficient, neutral density, and ambipolar diffusion coefficient are constant within the region being examined. By equating the diffusion losses with the ionization rate within the volume, the following equation for the plasma density can be obtained:

$$\nabla^2 n_e + \left(\frac{n_g \langle \sigma_{iz} v_e \rangle}{D_a} \right) n_e = 0. \tag{95}$$

The solution to this equation can be found using separation of variables. Assuming that there is no variation in the axial direction, the resulting plasma density is given by:

$$n_e(r) = n_e(0) J_0 \left(\sqrt{\frac{n_g \langle \sigma_{iz} v_e \rangle}{D_a}} r \right). \tag{96}$$

In order to solve for the electron temperature, Goebel and Katz assume that the electron density is zero at the wall of the cathode, yielding the final relationship between the ambipolar diffusion coefficient and the ionization rate coefficient in terms of the cathode geometry,

$$\left(\frac{r_c}{\lambda_{01}} \right)^2 n_g \sigma_{iz}(T_{eV}) \sqrt{\frac{8eT_{eV}}{\pi m}} = D_a, \tag{97}$$

where the ionization rate coefficient in Equation 97 has been replaced by the fit used by Mandell and Katz (Equation 23), and λ_{01} is the first root of the zeroth-order Bessel function of the first kind. This yields the radial variation in plasma density as well as the electron temperature. The average density, needed for later calculations, is given by:

$$\bar{n}_e = \left[\frac{2 J_1(\lambda_{01})}{\lambda_{01}} \right] n_e(0). \tag{98}$$

In an earlier paper, Katz *et al.*[43] state that the electron temperature calculated using this approach is the maximum possible value, and that the correction in T_{eV} for finite values of the separation constant is, "less than one per cent."

Current balance The current balance for the insert region equates the total discharge current with the sum of the emitted thermionic current and the generated ion current reduced by the random thermal electron current that returns to the emitter:

$$I_d = I_{em} + I_i - I_r \exp\left(-\phi_s / T_{eV}\right) \tag{99}$$

$$I_r = \frac{1}{4} \left(\frac{8eT_{eV}}{\pi m} \right)^{1/2} n_s e A_{\text{emit}} \tag{100}$$

$$I_i = n_g \bar{n}_e e \langle \sigma_{iz} v_e \rangle V_{\text{emit}} \tag{101}$$

Goebel and Katz also mention that the Bohm current is used to evaluate the ion current for the purposes of evaluating the ion power deposition, implying that $I_i = e n_s v_{\text{Bohm}} A_{\text{emit}}$ should also be valid by ion conservation, where n_s is the electron density at the sheath edge. The introduction of n_s is a unique feature of this model, as it is the only model that attempts to calculate the sheath voltage independent of the plasma potential. The random electron current density should also be evaluated at the sheath edge density. The ion generation, by contrast, should be evaluated using the average electron density, $\bar{n}_e$.

Power Balances The power balance for the insert plasma equates the power deposition from sheath-accelerated thermionic electrons and Ohmic heating to the losses due to ionization, electron convection, and random electron flux to the emitter:

$$I_{em}\phi_s + R_p I_e^2 = I_i \epsilon_i + \frac{5}{2} T_{eV} I_e + (2T_{eV} + \phi_s) I_r \exp\left(-\phi_s / T_{eV}\right) \tag{102}$$

The energy characteristic of the random electrons, $(2T_{eV} + \phi_s)$, is necessary because the particles must have sufficient energy to overcome the sheath potential. Otherwise the electrons would not leave the volume into the electron-repelling emitter sheath. A derivation of this term is also given in Appendix C of Ref. 11.

The power balance for the emitter sets the losses due to conduction, convection, and radiation ($H(T)$) and thermionic cooling equal to the power input by ion and random electron bombardment. Ions must extract an electron at the cost of the work function from the material in order to recombine at the emitter surface and incident electrons are assumed to fall from the vacuum level to the Fermi level within the material, depositing ϕ_w at the wall, as shown below:

$$H(T) + I_{em}\phi_w = I_i \left(\epsilon_i + \phi_s + \frac{T_{eV}}{2} - \phi_w\right) + (2T_{eV} + \phi_w) I_r \exp\left(-\phi_s / T_{eV}\right). \tag{103}$$

These equations cannot be readily solved as a system for the sheath voltage, plasma density, and wall temperature. They are instead combined to create simpler expressions that do not directly involve the wall temperature. This is achieved by assuming that the ion energy due to the pre-sheath can be neglected compared to the ionization and sheath potentials. This assumption does not typically introduce significant error given the 1-2 eV electron temperature characteristic of the insert plasma. Algebraic manipulation of the remaining equations and the introduction of an "edge-to-average" ratio f_n that describes the ratio of the average plasma density to that at the sheath edge, yields a system of equations that can be solved for the average neutral density and sheath voltage:

$$\phi_s = \frac{H(T)}{I_e} + \frac{5}{2} T_{eV} + \phi_w - R_p I_e, \tag{104}$$

$$\bar{n}_e = \frac{R_p I_e^2 - \left(\frac{5}{2} T_{eV} - \phi_s\right) I_e}{f_n T_{eV} \left(\frac{e T_{eV}}{2\pi m}\right)^{1/2} e A \exp\left(-\phi_s / T_{eV}\right) + n_g e \langle \sigma_{iz} v_e \rangle V \left(\epsilon_i + \phi_s\right)}. \tag{105}$$

The edge-to-average plasma density ratio is approximated by Goebel and Katz by assuming that the plasma density in the region outside the sheath and pre-sheath can be described by a Boltzmann distribution:

$$f_n = \frac{n_e}{\bar{n}_e} \approx \exp\left(-(\phi_{\text{axis}} - \phi_s)/T_{eV}\right). \tag{106}$$

Because this value represents the ratio of the plasma density at the sheath edge to the average density over the volume, an additional factor should be used to convert the average density to that at the centerline (following Equation 98) when calculating f_n. The plasma resistivity is calculated using Equation 28. The electron-ion collision frequency is evaluated with Equation 30 The electron-neutral collision cross-section is evaluated for xenon with a fit to Hayashi's[29] recommended *total* electron-neutral cross-section data (Equation 32). As mentioned earlier for Mandell and Katz's use of this model, the elastic momentum-transfer collision cross-section should be used instead. Goebel and Katz use Equation 64 as their definition of the Coulomb logarithm. In following the derivation of this model, we also found that the first term in the denominator of Equation 105 should be multiplied by a factor of 2.

These two equations must be solved iteratively or simultaneously for the average plasma density and the sheath potential, as the plasma resistance appears in the sheath potential equation and depends on the average plasma density. These values are both desirable, but because of the simplification, the model cannot predict the wall temperature directly. The dependence on the "edge-to-average" ratio requires the additional assumption that the plasma density follows a Boltzmann distribution (i.e., the density decays exponentially with potential) as well as knowledge of the plasma potential from either experimental data or 2-D codes in order to close the system. In addition, the equations for the average density and sheath voltage depend on the emitter heat loss, which must be found from either a separate thermal model or experiment, and the plasma resistivity, which is itself a function of the average plasma density and the emission length, L_{emit}.

The authors present a model for the emission or attachment length based on the "e-folding distance" for the plasma density decay. Relaxing the assumption of zero axial variation in density, the decay is assumed

to obey the earlier ambipolar diffusion model. To ensure uniform pressure and the validity of the ambipolar diffusion model, the cathode orifice must be relatively small compared to the insert diameter. An independent calculation of the ion current generated in the insert plasma is required, which the authors obtain through the use of a 2-D code, so this approach cannot be used in a self-contained fashion.

2. Orifice model

Goebel and Katz implement an additional power balance in a separate orifice model using the same flow and ambipolar diffusion models, assuming that the discharge current does not change within the orifice. It does not depend on experimental parameters as the attachment length is replaced with the orifice length, and emission from the orifice is ignored. This removes the need for the sheath potential in order to calculate the plasma density and electron temperature. The orifice power balance equates the Ohmic heating in the orifice to the electron convection losses and to the ionization power loss in the orifice volume:

$$I_d^2 R_{po} = \frac{5}{2}\left(T_{eV} - T_{eV}^{ins}\right) I_d + e n_g \langle \sigma_{iz} v_e \rangle \epsilon_i \left(\pi r_o^2 L_o\right). \tag{107}$$

This equation can be solved easily for the orifice average plasma density after the insert model has been run:

$$\bar{n}_e = \frac{I_d^2 R_{po} - (5/2) I_d \left(T_{eV} - T_{eV}^{ins}\right)}{e n_g \langle \sigma_{iz} v_e \rangle \epsilon_i \pi r_o^2 L_o}. \tag{108}$$

3. Evaluation

Overall, the model described above produces results that agree well with experiment when certain values of the input parameters are used. The model requires experimental/computational input in the form of the plasma potential and the attachment length (or the ion current, which can then be used to calculate L_{emit}). The results of the original model, our reimplementation, and the experimental data that Goebel and Katz compare with are shown in Figure 16. Our reimplementation uses a gas temperature of 4000 K in order to be consistent with the insert model inputs, a constant plasma potential of 8.5 V, and a constant heat loss of 13 W. Goebel and Katz's original implementation uses a gas temperature of 2000 K.

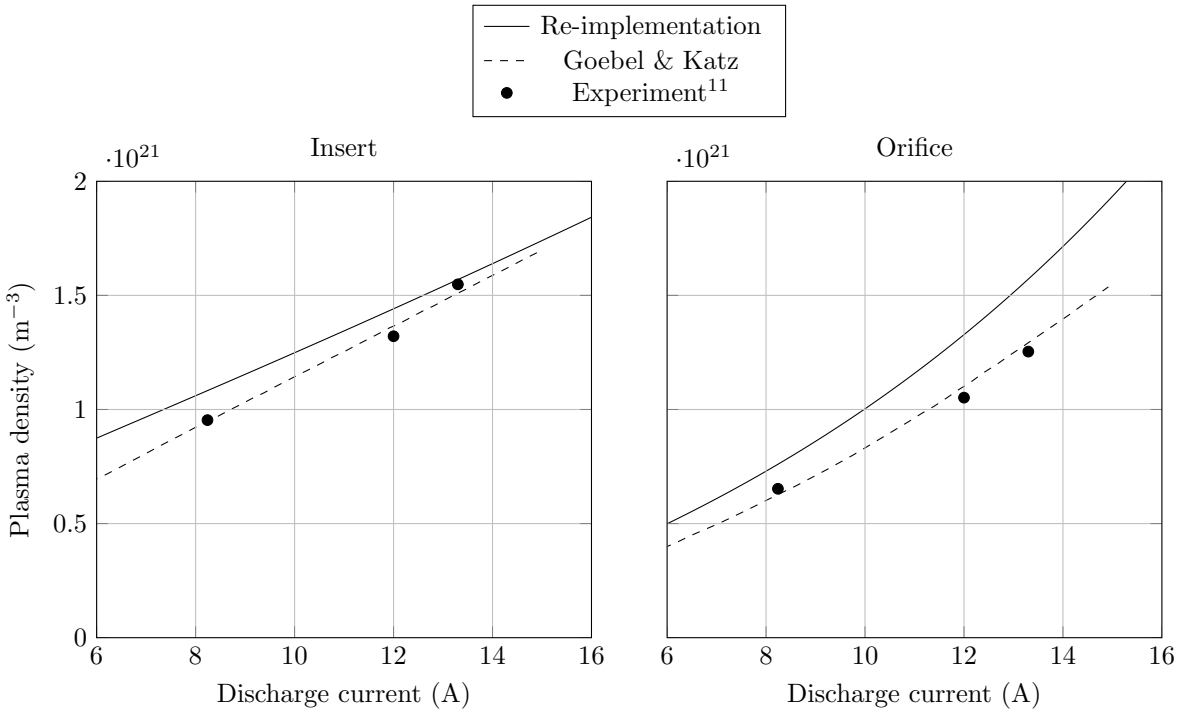

Figure 16. Comparison of original and re-implemented model using Goebel and Katz's approach. Experimental data is from Ref. 11. No error bars are reported.

Goebel's model has two independent equations for the ion current. This can be used to make a secondary calculation of the edge-to-axis density ratio and the insert electron temperature. Equating the Bohm and ion generation forms of the ion current within the insert, we can solve for the electron temperature and f_n as functions of only the pressure-diameter product in the insert, as shown in Figure 17. Using this approach (not used by the original authors), we can remove the need for the plasma potential, as it is only used to calculate f_n. It is important to note that the ambipolar diffusion model as formulated breaks down at low pressure-diameter products or at high electron temperatures (typical for orifice plasma conditions), either because of the lack of electron-ion collisions or due to the boundary conditions of the diffusion model. For orifice conditions, f_n approaches values of unity (or greater) and therefore the assumption of zero plasma density at the sheath edge cannot be justified.

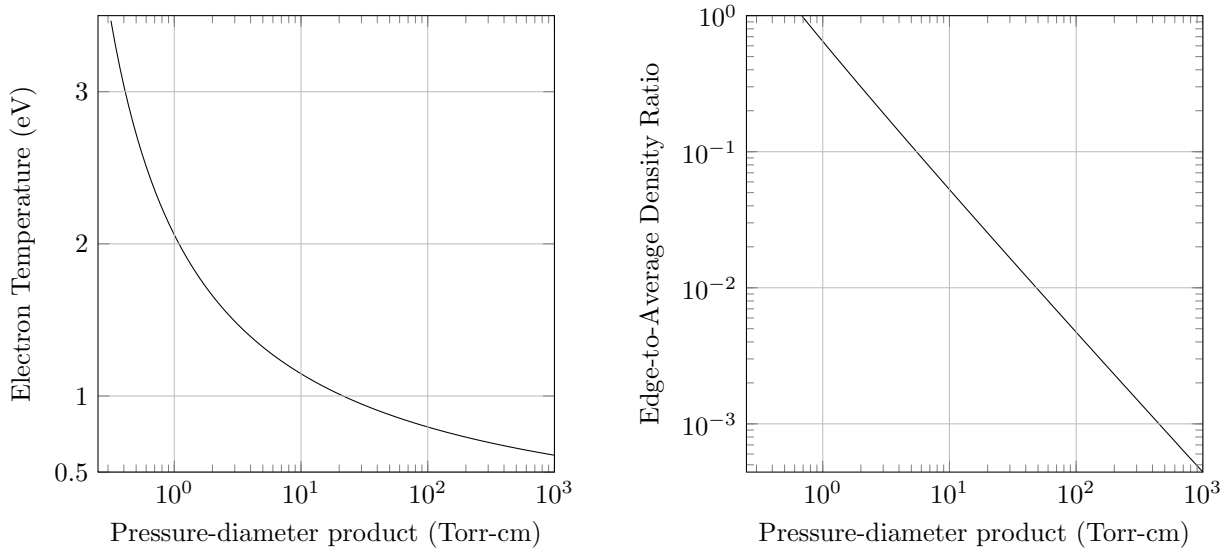

Figure 17. Electron temperature and edge-to-average plasma density ratio as functions of pressure-diameter product, where the neutral gas temperature is assumed to be 4000 K and the pressure is assumed to be the neutral gas pressure.

G. Mizrahi *et al.*[46,47]

Mizrahi *et al.*'s model is only concerned with the hollow cathode orifice during operation. It is loosely based on Katz's model, and introduces the following modifications:

- The plasma is allowed to flow along the length of the orifice.
- The neutral gas temperature is equal to the ion temperature. Both heavy species temperatures are assumed to be much less than the electron temperature.
- Viscous effects on the neutral gas flow are introduced through a Poiseuille flow model.
- Ions may leave the cathode by being entrained by the neutral flow.

This approach relies on the continuity and momentum equations for charged particle flow, a plasma energy balance in the volume, and a neutral gas flow model. The superscripts $i \pm 1/2$ in this section refer to the physical quantities evaluated at the right- and left-hand sides of the volume, respectively.

Neutral flow A Poiseuille flow approach is used to evaluate the neutral gas density in the orifice. The Poiseuille equation is manipulated so as to introduce the arithmetic average density $\bar{n}_g = 1/2\left(n_g^{i+1/2} + n_g^{i-1/2}\right)$

$$\bar{u}_g = \frac{\Delta P r_o^2}{8\mu L_o} \Leftrightarrow \bar{u}_g = \frac{1-\delta}{1+\delta}\frac{k_B T_g \bar{n}_g r_o^2}{4\mu L_o}, \tag{109}$$

where

$$\Delta P = k_B T_g \left(n_g^{i-1/2} - n_g^{i+1/2} \right), \text{ and} \tag{110}$$

$$\delta = n_g^{i+1/2} / n_g^{i-1/2}. \tag{111}$$

This form of the Poiseuille equation removes the necessary knowledge of the upstream and downstream pressure, at the cost of the introduction of a free parameter, δ. The free parameter δ may be estimated if the neutral gas pressure and temperature are known downstream and upstream of the orifice:

$$\delta = n_g^{i+1/2} / n_g^{i-1/2} = T_{gV}^{i+1/2} P^{i+1/2} / T_{gV}^{i-1/2} P^{i-1/2}. \tag{112}$$

If we further assume that the neutral temperature is constant along the orifice, then:

$$\delta = P^{i+1/2} / P^{i-1/2}. \tag{113}$$

The knowledge of the pressure downstream or upstream of the orifice, and the application of a Poiseuille flow model, yields the missing pressure, and δ.

Charged particle flow The momentum equations are written for both ions and electrons. The electron velocity is considered to be dominant over the ion and neutral velocities, and the ion-neutral collision term dominates over the ion-electron term in the ion momentum equation. The authors consider a steady-state system, and neglect the convective derivative. The neutral velocity is implicitly assumed to be the average neutral gas flow velocity in the channel from Equation 109. The combination of both the electron and ion momentum equations yields:

$$n_e u_i = n_e u_g - D_a \nabla n_e - \frac{m}{M} \frac{\nu_{ei} + \nu_{en}}{\nu_{in}} n_e u_e. \tag{114}$$

The authors argue that the third term is negligible since $\frac{m}{M} \frac{\nu_{ei}+\nu_{en}}{\nu_{in}} \ll 1$, in direct contradiction with Katz *et al.*[48] This assumption does not take into account the electron velocity as compared to the ion or neutral velocities. We can evaluate the first and third term on the right-hand side of Equation 114. The neutral flow velocity is given by Equation 109. The electron flow velocity may be calculated by considering all of the discharge current to be carried by the electrons $I_d = e n_e \pi r_o^2 u_e$. We used Equation 30 for the electron-ion collision frequency, and the Maxwellian-averaged momentum-transfer cross-section for electron-neutral collisions from Hayashi (Ref. 31) to calculate the electron-neutral collision frequency $\nu_{en} = n_g \langle \sigma v \rangle$. The charge-exchange collision cross-section is assumed to be equal to 10^{-18} m^2. Using the reported results of the model for xenon gas ($n_g = 1.1 \times 10^{23}\,\mathrm{m}^{-3}$, $n_e = 2.7 \times 10^{22}\,\mathrm{m}^{-3}$, $T_{eV} = 1.6\,\mathrm{eV}$, $T_{iV} = 0.4\,\mathrm{eV}$), both the third and first term on the right-hand side of Equation 114 may be evaluated:

$$\frac{m}{M} \frac{\nu_{ei} + \nu_{en}}{\nu_{in}} u_e \approx 170\,\mathrm{m/s}$$

$$u_g \approx 181\,\mathrm{m/s}$$

Clearly, the electron current term cannot be neglected based on the results of the model.

Density evaluation The density in the 0-D cell is considered to be constant and equal to the average value. The cell-center density is also expected to be much greater than the density at the cell boundaries, due to significant ionization within the constricted orifice and expansion to vacuum at the outlet.

The density gradient in Equation 114 can be evaluated through a Taylor expansion from the center density to the boundary,

$$\nabla n_e = \frac{\partial n_e}{\partial z}\Big|_{i\pm1/2} \approx \frac{\mp n_e^i \pm n_e^{i\pm1/2}}{L_o/2} \approx \mp \frac{n_e^i}{L_o/2}. \tag{115}$$

The authors consider the center density n_e^i to be equal to the average density within the cell, $\bar{n}_e$, which gives:

$$\frac{\partial n_e}{\partial z}\Big|_{i\pm1/2} \approx \mp \frac{\bar{n}_e}{L_o/2}. \tag{116}$$

A similar approach can be taken to evaluate the density gradient in the radial direction.

In the axial direction, by virtue of Bolzano's theorem, the gradient of the density must be zero at least once on the interval $\left[z_{i-1/2}, z_{i+1/2}\right]$. If this density maximum is achieved at the center of the cell, the density over the whole cell should be equal to $\bar{n}_e$ to be consistent with the average density definition. This approach yields a discontinuity in density at the boundaries of the cell. For example, $n_e^{i-1/2,L} \neq n_e^{i-1/2,R}$ since $n_e^{i-1/2,L} \ll n_e^{i-1/2,R}$, where L and R designate the limited values when approached from the left and right-hand sides of the boundary, respectively. Other cases require sharp density gradients in the first half or second half of the cell for consistency.

Continuity equation The mass flow rate for neutrals is obtained from the volumetric mass flow rate $Q = \bar{u}_g \pi r_o^2$ using:

$$\dot{m}_g = M n_g \pi r_o^2 \bar{u}_g. \tag{117}$$

The ion mass flow rate is obtained in a similar fashion:

$$\dot{m}_i = M n_e \pi r_o^2 u_i. \tag{118}$$

For both boundaries, we have

$$\dot{m} = \dot{m}_g + \dot{m}_i = M\pi r_o^2 \left(\bar{u}_g n_g^{i\pm1/2} + (u_i n_i)^{i\pm1/2}\right). \tag{119}$$

Averaging the value at left and right boundaries, and combining it with Equation 114 yields:

$$\dot{m} = M\pi r_o^2 \left(\bar{n}_g + \frac{1}{2}\left(n_e^{i+1/2} + n_e^{i-1/2}\right)\right)\bar{u}_g. \tag{120}$$

The authors are inconsistent with the density definition, and assume that $\bar{n}_e = \frac{1}{2}\left(n_e^{i+1/2} + n_e^{i-1/2}\right)$, though the boundary plasma densities have previously been assumed to be negligible compared to the average density ($\bar{n}_e \gg n_e^{i\pm1/2}$). The resulting mass conservation equation is:

$$\dot{m} = M\pi r_o^2 \left(\bar{n}_g + \bar{n}_e\right)\bar{u}_g. \tag{121}$$

Radial diffusion The radial diffusion of ions is assumed to be governed by charge-exchange collisions. The corresponding radial flux is evaluated in the same fashion as the axial boundary flux:

$$J_i = -eD_a \frac{\partial \bar{n_e}}{\partial r}\Big|_{r=r_o} \approx eD_a \frac{n_e}{r_o}. \tag{122}$$

In contrast with that of Goebel and Katz, this approach does not consider sheath physics and uses a linearized density gradient.

Ion balance Ions are considered to be created in the volume through direct-impact ionization with thermalized electrons, and are lost through diffusion to the boundaries. The ion balance is similar to that of all of the previously described authors. Using the axial and radial diffusion approach, the ion balance is given by:

$$\pi r_o^2 \left(J_i^{i+1/2} - J_i^{i-1/2}\right) + 2\pi r_o L_o J_i^{r=r_o} = \pi r_o^2 L_o e \bar{n}_g \bar{n}_e \sigma_{iz}\left(T_{eV}\right)\sqrt{\frac{eT_{eV}}{m}}$$
$$\Leftrightarrow \bar{n}_g \sigma_{iz}\left(T_{eV}\right)\sqrt{\frac{eT_{eV}}{m}} = \frac{2D_a}{r_o^2}\left(1 + 2\left(r_o/L_o\right)^2\right). \tag{123}$$

Although Mizrahi *et al.* use the electron thermal velocity, Mandell and Katz's fit uses the Maxwellian velocity for the electrons.

Power balance The power balance is similar to that of previously described authors. Mizrahi *et al.* do not consider a double-sheath, but consider Ohmic heating balanced by ionization, excitation, and convection. Plasma resistance is provided through electron-ion and electron-neutral collisions. The cross-sections for electron-neutral collisions, ionization, and excitation are estimated with numerical fits (Equations 32, 23 and 27, respectively):

$$R_p I_d^2 = \pi r_o^2 L_o \bar{n}_g \bar{n}_e e \sqrt{\frac{eT_e V}{m}}\left(\epsilon_i \sigma_{iz} + \epsilon_{ex}\sigma_{ex}\right) + \frac{5}{2}\left(T_{eV} - T_{eV}^{\text{ins}}\right) I_d. \tag{124}$$

ALGORITHM The model consists of three equations — neutral gas flow (Equation 121), ion conservation (Equation 123), and plasma power balance (Equation 124). The unknowns are the electron temperature, average electron density, and average neutral gas density. It is necessary to know the operating conditions ($\dot{m}$ and I_d), cathode geometry (L_o , r_o), gas used (cross-sections, mass, and ionization and excitation energies), insert electron temperature, ion temperature, and free parameter δ.

EVALUATION Despite several fundamental inconsistencies, the model performs relatively well on the NSTAR neutralizer cathode as compared to other 0-D and higher-dimensional models. Mizrahi *et al.*'s model unfortunately relies on a free parameter, and on experimental data for the insert electron temperature. The study does not feature a sensitivity analysis.

We reproduced the results of Mizrahi *et al.* by first calculating the specified insert electron temperature using Equation 124 and the reported data from Ref. 47. A value of $T_{eV}^{\text{ins}} = 0.46$ eV was found. We used this value for the rest of our calculations. The expression for the charge-exchange collision cross-section used by the authors in Ref. 47 is not clear. We used a constant value of $\sigma_{\text{CEX}} = 10^{-18}$ m^2. We accurately reproduced Mizrahi *et al.*'s results for the specified cathode (NSTAR — $L_o = 0.75$ mm, $r_o = 0.14$ mm), gas (Xenon), operating conditions ($\dot{m} = 3.6$ sccm, $I_d = 3.26$ A), and additional free parameters ($\delta = 0.2$, $T_{eV}^{\text{ins}} = 0.46$ eV, $T_{gV} = T_{iV} = 0.4$ eV). Numerical values are shown in Table 1, along with results from Mandell and Katz's model. Mizrahi *et al.* also performed calculations using Mandell and Katz's model, but set the neutral gas temperature equal to that of the electrons. Results from both approaches (with $T_{gV} = T_{eV}$ or $T_{gV} = 0.1$ eV) are presented.

Model	n_e ($\times 10^{-22}$ m^{-3})	n_g ($\times 10^{-23}$ m^{-3})	T_{eV} (eV)	$\alpha = n_e/(n_e + n_g)$
Mizrahi *et al.* (Ref. 47)	2.7	1.1	1.6	0.2
Reproduction of Ref. 47	2.45	1.15	1.61	0.18
Mandell and Katz (Ref. 25) $T_{gV} = T_{eV}$	0.91	0.43	2.18	0.17
Mandell and Katz (Ref. 25) $T_{gV} = 0.1$ eV	1.45	1.82	1.74	0.07

Table 1. Comparison of original results from Ref. 47 to the reproduced model and to Mandell and Katz' model

The results from all of the models are consistent with each other, though Mandell and Katz's model with a reasonable temperature implementation ($T_{gV} = 0.1$ eV) predicts an ionization fraction 3 times lower than the other models. No comparison to experimental data is presented in Ref. 47, or available in the literature.

H. Albertoni et al.[9, 14, 49, 50]

Albertoni proposes a model for the insert and orifice plasmas. The orifice is modeled as a separate 0-D volume.

A free-standing double sheath at the orifice entrance is assumed to be present, which accelerates electrons towards the orifice while keeping ions within the emitter region. Albertoni's orifice model includes an ion flux balance, plasma power balance, and a choked-flow calculation to compute plasma density, electron temperature, and neutral density in the orifice region. Processes such as excitation — and therefore step-wise ionization — and radiation are neglected.

The emitter region model includes an ion flux balance, plasma and emitter power balances, a current density balance, and a pressure equation. Albertoni's model considers thermal and emitted electrons as well as ions for the current balance. Volume ionization is again considered to originate from thermalized Maxwellian electrons, while step-wise ionization is neglected. The model must be coupled with a thermal simulation to obtain the temperature of the emitter, and therefore the emitted current. An early version of this model[9] that ignored the orifice showed good agreement for the peak emitter wall temperature for a single-channel hollow cathode. The current model predicts the variation of the plasma potential with mass flow rate and discharge current, but the author notes that these can not be compared with readily available experimental data. Albertoni's analysis neglects the emitted electrons, which participate in the step-wise ionization and neutral excitation processes, and suffers from the necessity of a coupled thermal model, which further complicates the solution process. The thermal model also considers that the emitter temperature is

uniform, while experimental measurements have shown that emitter temperatures may vary by more than 10% of the peak temperature.[51,52]

In an early version of his model, Albertoni carries out a separate evaluation of the plasma attachment length by invoking the "principle of minimum power," which seeks to minimize the power deposited in the sheath $P_s = I_d\phi_s$, and therefore the sheath voltage ϕ_s for a given current. Albertoni solves the 0-D model by iterating through multiple plasma attachment lengths, and finds the corresponding minimum in the sheath voltage. For a given discharge current, minimizing the sheath voltage amounts to minimizing the net current density, which may bias this method towards the prediction of longer attachment lengths. Numerical results for the plasma attachment length scale inversely with mass flow rate, as observed experimentally, but predict that L_{emit} increases with the discharge current, in contradiction with experimental results.[11,53]

1. *Orifice model*

Albertoni's approach is very similar to that of Domonkos: ion conservation and a plasma power balance are considered, achieving closure through a modified choked-flow pressure relation.

Ion conservation The ion conservation equation is identical to Equation 47. The author uses the Bohm criterion for the ion current density,

$$J_i = 0.61 e n_e \left(\frac{eT_{eV}}{M}\right)^{1/2}. \tag{125}$$

Plasma volume power balance Albertoni uses the total discharge current in the Ohmic heating term, and introduces a double-sheath power loss which is subsequently neglected. Power losses due to excitation of neutrals and radiation are also neglected:

$$\dot{q}_\Omega = \dot{q}_{iz} + \dot{q}_{ex} + \dot{q}_{\text{conv}} + \underbrace{\dot{q}_{ds}}_{\text{neglected}} \tag{126}$$

The ionization power, $\dot{q}_{iz}$, is expressed as in Equation 12 and the ionization rate is found as in Domonkos's model (Equation 48).

Albertoni does not consider the current to vary along the length of the orifice, so the total discharge current is used in the Ohmic heating term,

$$\dot{q}_\Omega = R_p I_d^2. \tag{127}$$

The resistance of the plasma is obtained with both electron-ion and electron-neutral collisions. The electron-neutral collision cross-section is estimated from Equation 32 (Ref. 28), while the collision frequency is estimated using the thermal velocity of the electrons, as opposed to the Maxwellian average velocity. The convection power is estimated as in Equation 68, but using a factor of 2 (which, once again, should be 5/2).

Pressure calculation Closure of the system is obtained through a choked-flow model of the orifice region, modified to account for the contribution of electrons to the flow:

$$P = \frac{\dot{m}}{\pi r_o^2}\sqrt{\frac{R}{\gamma}T_g\left(1+\alpha\frac{T_e}{T_g}\right)}. \tag{128}$$

All quantities are considered to be static rather than stagnation properties. The gas temperature is assumed to be equal to that of the orifice plate. The total static pressure is equated to that given by the perfect gas law (Equation 3).

The correction for the electron pressure contribution is equivalent to calculating an effective gas constant for a mixture of heavy particles and electrons, assuming that T_e is constant and that all species expand isentropically through the orifice. For monatomic species, the total enthalpy of the fluid mixture may be

expressed as:[54]

$$\begin{aligned} h_{\text{total}} &= \frac{n_e m}{n_e m + n_g M}\left(\frac{5}{2}\frac{k_B T_e}{m} + \frac{n_g M}{n_e m}\frac{5}{2}\frac{k_B T_g}{M}\right) \\ \Leftrightarrow h_{\text{total}} &\approx \alpha\frac{5}{2}\frac{k_B T_e}{M} + \frac{5}{2}\frac{k_B T_g}{M} \\ \Leftrightarrow h_{\text{total}} &\approx \frac{5}{2}\underbrace{\frac{k_B}{M}\left(1+\alpha\frac{T_e}{T_g}\right)}_{\text{Effective gas constant}} T_g \end{aligned} \tag{129}$$

2. Insert model

The insert model features ion conservation, current conservation, plasma power balance, and pressure balance equations.

Ion conservation Albertoni considers that ions are brought into the control volume through direct ionization and from the orifice through the double sheath. Ions are lost through the sheaths, and thermally upstream. The resulting ion balance is given by:

$$e\left(\frac{dN_i}{dt}\right)_{\text{iz}} + J_i^{ds}\pi r_o^2 = J_i\left(2\pi r_c L_{\text{emit}} + \pi(r_c^2 - r_o^2)\right) + \frac{1}{4}n_e e\sqrt{\frac{8eT_{iV}}{\pi M}}\pi r_c^2. \tag{130}$$

Orifice and insert quantities are used to calculate J_i^{ds} and J_i, respectively. They are both given by Equation 125. The use of the Bohm current for the double sheath ion current leads to the previously discussed issues regarding the double sheath voltage and power predictions.

Current conservation Albertoni includes neither ion nor electron losses to the orifice plate, nor does he include thermal ions lost through the upstream boundary of the volume for current conservation, though the contribution of these terms to the discharge current is likely small. The resulting current balance at the emitter surface is given by:

$$\frac{I_d}{2\pi r_c L_{\text{emit}}} = J_i + J_{em} - J_r \exp\left(-\frac{\phi_p}{T_{eV}}\right). \tag{131}$$

The thermionic current J_{em} is calculated with Equation 8. J_r is obtained with Equation 84. Using the total discharge current in this expression neglects the contribution of the orifice ions to the total current.

Plasma power balance The plasma power balance is similar to Equation 85, though Albertoni does not consider losses due to neutral excitation.

$$\dot{q}_\Omega + \dot{q}_{\text{ori}} + \dot{q}_{em} = \dot{q}_{iz} + \dot{q}_{\text{conv}} + \dot{q}_{\text{coll}}. \tag{132}$$

$\dot{q}_\Omega$, $\dot{q}_{\text{ori}}$, $\dot{q}_{em}$, $\dot{q}_{iz}$ are given by Equations 87, 88, 89, and 90, respectively. Albertoni's expression for $\dot{q}_{\text{coll}}$ is similar to that of Equation 92, though the author does not include the plasma potential in the total energy of the collected electrons (electrons leaving the plasma in this case):

$$\dot{q}_{\text{coll}} = \left(I_i^{th} + I_i^{\text{coll}}\right)2T_{iV} + I_e^{\text{coll}}2T_{eV}. \tag{133}$$

This is a substantial omission for significant return electron currents. The power convected by the electron current is:

$$\dot{q}_{\text{conv}} = \frac{5}{2}T_{eV}I_d. \tag{134}$$

Neutral flow The system is closed with a pressure balance similar to that of Domonkos. Albertoni's formulation as reported in Ref. 14 is dimensionally inconsistent, as the radius should appear to the fourth power. Albertoni calculates the dynamic viscosity from kinetic theory, considering hard-sphere particles of diameter d_m and a mean-free-path approach:

$$\mu = \frac{1}{\pi d_m^2}\sqrt{\frac{Mk_B T_o}{\pi}}. \tag{135}$$

A comparison of the viscosity calculations for the hard-sphere approach, the Chapman-Enskog method applied to the Lennard-Jones 12-6 potential with $\sigma = 4.055\,\text{Å}$ and $\epsilon/k_B = 229$ K, and a derivation of viscosity from dimensional analysis from Stiel and Thodos[55] is shown for xenon in Fig. 18. The Van der Waals radius for xenon is considered to be equal to 216 pm for the hard-sphere model. The collision integrals for the Chapman-Enskog calculations are tabulated in Ref. 56 and originally from Ref. 57. The hard sphere model under predicts the viscosity at high-temperatures, which is especially important in the orifice. The Lennard-Jones 12-6 potential yields very close agreement to the experimental fit. We suggest using either the fit to experimental data or the Lennard-Jones potential approach for accurate calculation of the viscosity.

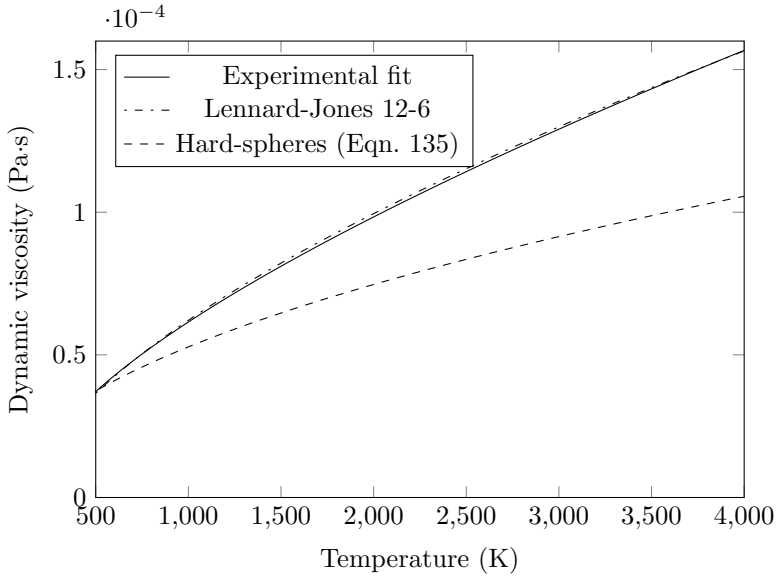

Figure 18. Comparison of three different viscosity models.

THERMAL MODEL Albertoni includes a thermal model to predict the emitter temperature. Convection from the insert, conduction through the cathode tube, radiation from both the heat shield and orifice surfaces, and heat dissipation through evaporation of the insert are considered. The plasma processes at the insert surface deposit power through ion bombardment and electron backstreaming, and contribute to cooling through thermionic emission. Ohmic power deposition in the orifice plasma is assumed to be entirely transferred to the orifice plate. For radiation, a background temperature of 0 K is assumed. The base of the cathode is kept at an arbitrary value of 1000 K.

Albertoni represents the cathode as a radiative thermal network (see Figs. 4 and 5 in Ref. 14). The radiosities J_k are unknown, as are the node temperatures. The thermal network requires the power inputs and outputs to the insert node, which are obtained from the insert power balance.

INSERT POWER BALANCE Albertoni's insert power balance is similar to that of Goebel and Katz. The author does not consider the pre-sheath contribution to the ion power — though he uses the Bohm sheath criterion for the ion current — and adds the emitter temperature to the total energy of the emitted electrons. The emitter temperature contribution is negligible compared to the effective work function.

$$\dot{q}_{th} + I_{em}\left(\phi_{\text{eff}} + \frac{3k_B}{2e}T_c\right) = I_i\left(\epsilon_i + \phi_p - \phi_w\right) + \left(2T_{eV} + \phi_w\right) I_r \exp\left(-\frac{\phi_p}{T_{eV}}\right). \tag{136}$$

The plasma model is coupled to the thermal model through the heat loss term, $\dot{q}_{th}$.

EMISSION LENGTH In Ref. 14, the plasma attachment length is calculated with an empirical argument. Albertoni proposes that the product of the pressure and the attachment length is equal to a constant between 5 and 15 Pa·m, similar to the result for single-channel hollow cathodes:

$$K \approx PL_{\text{emit}},\ K = 5 - 15\text{Pa}\cdot\text{m}. \tag{137}$$

The constant K is used as a free parameter.

We compared the emission length obtained from Equation 137 to experimental data from Ref. 16. The pressure is calculated using Equation 4. The cathode considered is Siegfried and Wilbur's noble gas cathode operating on xenon and argon at mass flow rates of 92 and 287 mA, respectively. The orifice diameter for this cathode is 0.76 mm. Results are shown in Fig. 19.

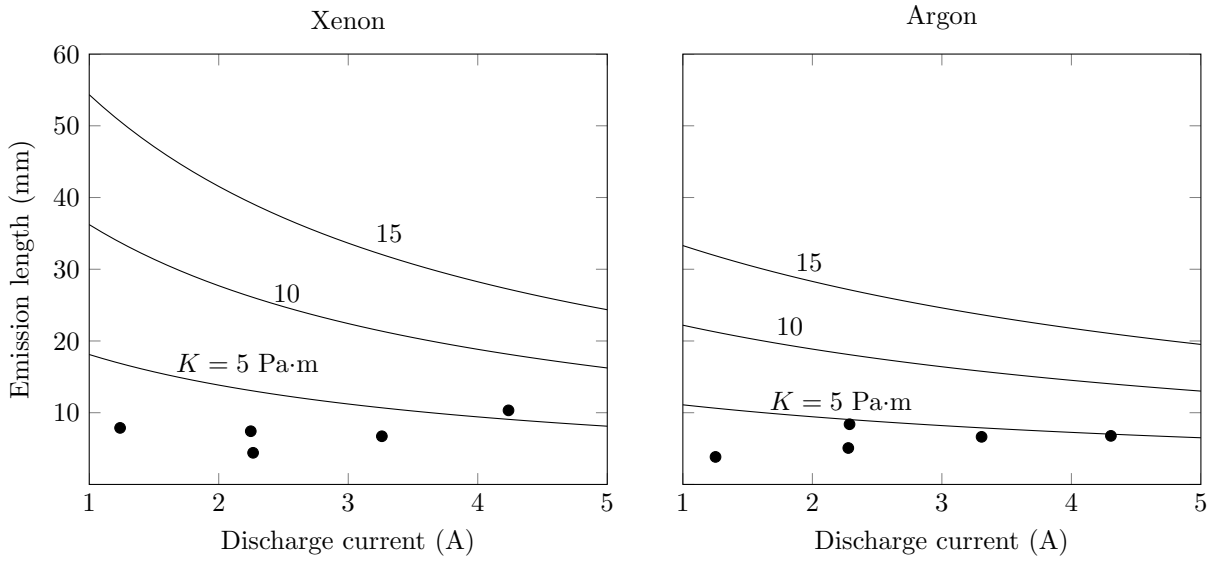

Figure 19. Comparison of emission length empirical relationship (Equation 137) for $K = 5, 10, 15$ Pa·m to experimental data from Ref. 16.

A value of K outside the specified range would clearly be required to achieve agreement with experimental results.

3. Evaluation

Algorithm The solution procedure is iterative; after initialization, the orifice, emitter, and thermal models are computed sequentially until convergence is obtained on the insert electron temperature, gas temperature, and cathode wall temperature. The effective length is then adjusted. Iterations continue until the effective length converges. Figure 6 from Ref. 14 shows a flow-chart of the algorithm.

Application The model does require additional information — material properties, further geometric data, and gas information. However, it is self-contained and does not require any experimental data other than collisional cross-sections (unless L_{emit} is fit to the experimental data). It solves for the neutral and electron densities, plasma potential, and orifice and insert temperatures. Due to the complexity and detailed requirements for property input for Albertoni's thermal model, we were not able to reimplement this model.

III. Comparisons

We benchmarked the performance of the models on cathodes with readily available experimental data and a heat loss estimate, a necessity for the insert models. This data is available for Siegfried and Wilbur's original xenon cathode, and the NSTAR discharge cathode. Siegfried and Wilbur's cathode uses a tantalum insert coated with R-500 (a barium-strontium-carbonate mixture[10]) as an emitter, while the NSTAR discharge cathode uses a porous tungsten insert impregnated with a mixture of barium, calcium, and aluminum oxides.[11] The dimensions for the different benchmark cathodes are shown in Table 2. We included the NEXIS cathode as it will be used in the next section for flow model comparisons.

Cathode	Dimension					
	Insert			Orifice		Tube
	L (cm)	I.D. (cm)	O.D. (cm)	L (mm)	D (mm)	D (cm)
Siegfried and Wilbur[16, 23]	1.5 – 2.0	0.39	0.40	1.8	0.51 – 0.96	0.63
NSTAR Discharge[11, 33, 43, 58–61]	2.54	0.38	0.55	0.74	1.02	0.635
NEXIS[11, 60, 62–64]	2.54	1.2*	1.42†	0.74‡	1.5 – 2.8	1.5

* The insert inner diameter is set to 1.20 cm, following Mikellides *et al.*'s work.[60, 62, 63] Later work by Goebel and Katz[11] suggests an insert diameter of 1.27 cm.

† The outer diameter for the NEXIS cathode is deduced from insert thickness data retrieved from Refs. 63 and 60.

‡ Measured from plots in Ref. 60.

Table 2. Dimensions of the benchmark cathodes.

A. Siegfried and Wilbur's xenon cathode

We considered the cathode with an orifice diameter of $d_o = 0.76\,\text{mm}$, running on xenon at a mass flow rate of 92 mA (1.28 sccm of xenon, or 0.13 mg/s). We varied the input discharge current from 1 to 5 A, and compared outputs of the two recreated insert models to experimental data.

1. *Required inputs*

The heat loss term necessary for both recreated insert models is obtained from Ref. 16:

$$\dot{q}_{th} = 2\big(526T_c - 3.99 \times 10^5\big) L_{\text{emit}} r_c \tag{138}$$

Siegfried assumes a value of 0.8 eV for the electron temperature in the insert.[16] We used this value in all of the calculations that require an insert electron temperature. We have also used the total inelastic cross-section data given by Wilbur[16] for the calculation of the energy-exchange mean free path to avoid calculating a new value of the proportionality constant between λ_{pr} and L_{emit}.

Goebel and Katz's insert model requires insert wall temperature, emission length, and plasma potential. We used experimental data available in Ref. 16. The neutral gas temperature is set equal to twice the measured wall temperature.

Siegfried notes that the work function of the R500-coated tantalum insert is unknown, and assumes a value of 2.25 eV — we used this value for our calculations. We set the orifice neutral temperature to 0.4 eV for Mandell and Katz's orifice model and for that of Mizrahi *et al.*. The free parameter δ in Mizrahi *et al.*'s orifice model is set to 0.2 for this cathode.

2. *Comparison*

Results for the insert and orifice models are shown in Figs. 20 and 21, respectively.

Our re-implementation of Siegfried and Wilbur's model is able to recreate their original results. The curvature changes observed on both implementations originate from the total inelastic cross-section for xenon that appears in the emission length calculation. Goebel and Katz's insert model overestimates the plasma density in the insert region by a factor of 5, though the model is very sensitive to the input plasma potential, emission length, and estimated heat loss. No error bounds are provided for these values.

The orifice models yield consistent results for the plasma density. Both Goebel and Katz's and Mizrahi *et al.*'s results for the electron temperature are insensitive to the discharge current, with Goebel and Katz's estimate being the largest value consistent with the assumptions of their model. Mandell and Katz's model returns a substantially larger ionization fraction as compared to the other models. However, without experimental data for the orifice, it is difficult to determine which model is the most accurate.

B. NSTAR discharge cathode

We computed averaged quantities for the NSTAR discharge cathode operating at the mass flow rates specified by the "TH8" and "TH15" operational conditions. TH8 and TH15 differ both in terms of mass flow rate and discharge current (see Table 3).

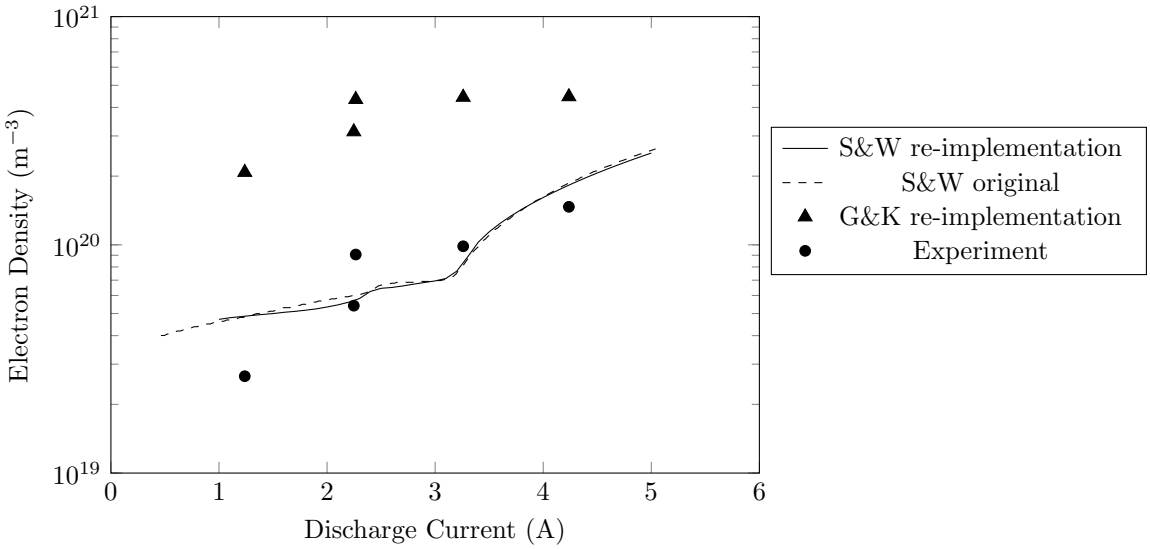

Figure 20. Comparison of cathode insert models for Siegfried and Wilbur's xenon cathode. Experimental data and original model results are from Ref. 16

1. Required inputs

We computed the average electron temperature and plasma potential in the insert region from experimental data obtained from Ref. 65. The heat loss term necessary for the insert models is taken to be a constant value of 13 W. This figure is taken from the results of the application of the thermal model IROrCa2D on the NSTAR cathode.[59] Though the application point for Ref. 59 ($I_d = 12$ A, $\dot{m} = 4.25$ sccm) differs from the two considered operational points, we follow Ref. 11 and use this value for all operating conditions. The operating conditions and required inputs are delineated in Table 3.

Parameter		TH8	TH15
Operating condition	I_d (A)	8.24	13.3
	$\dot{m}$ (sccm)	2.47	3.7
Experimental data	$\bar{\phi}_p$ (V)	9.2	5.5
	$\bar{T}_{eV}$ (eV)	1.4	1.4

Table 3. Operating conditions and average experimental data required for model input. The definition of the TH8 and TH15 operating points is taken from Ref. 61. The average plasma potentials and electron temperatures are computed from Ref. 65 — the reported measurement error is ±1 V for the potential, and ±0.5 eV for the electron temperature.

We used a work function equal to 2.06 eV for the insert material. The experimental data for the total pressure reported in Ref. 65 is used in Siegfried and Wilbur's insert model. The orifice models use an assumed insert electron temperature, which is set equal to the average value of 1.4 eV. The neutral gas temperature is assumed to be equal to 0.4 eV. Goebel indicates that the downstream pressure at the exit plane of the orifice on the NSTAR discharge cathode is approximately 2 Torr.[11] Using a Poiseuille flow model, we calculated the upstream pressure for the two specified mass flow rates. The resulting values for δ are 0.31 and 0.26 for $\dot{m} = 2.47$ sccm and $\dot{m} = 3.7$ sccm, respectively.

2. Comparison

Insert and orifice results are shown in Tables 4 and 5, respectively. For low current conditions, both Siegfried and Wilbur's and Goebel and Katz's insert models agree with experimental data. The ionization fraction for Siegfried and Wilbur's model is three times lower than the experimental value, but it is not clear if this result lies outside of the error bounds. For the high current condition, Siegfried and Wilbur's insert model

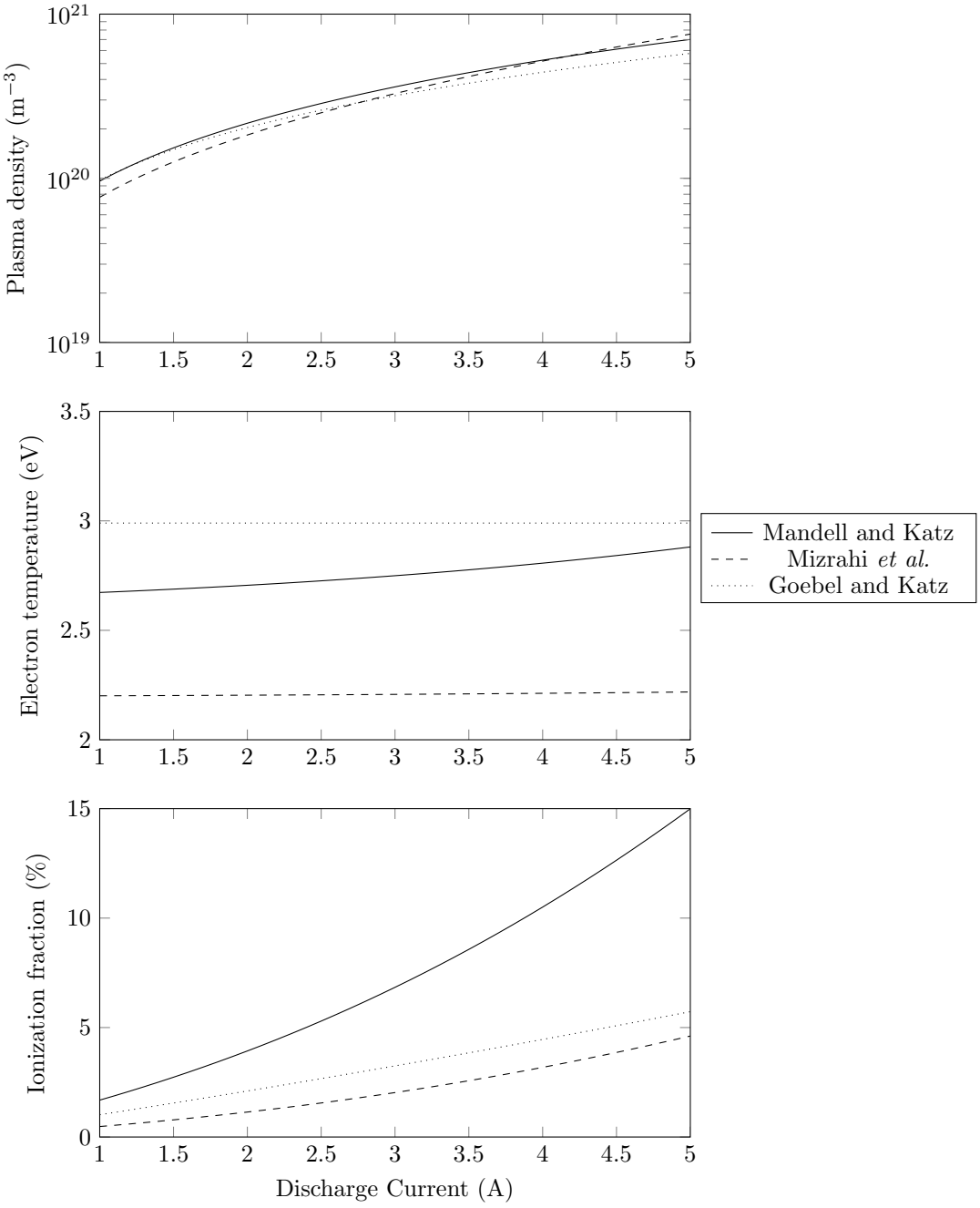

Figure 21. Comparison of cathode orifice models for Siegfried and Wilbur's xenon cathode.

over predicts the plasma potential, a consequence of their neglecting Ohmic heating, return electron current, and assuming $\phi_s = \phi_p$. This model does predict a lower attachment length at higher current and mass flow rate, consistent with experimental observations, and shows great accuracy for the emitter temperature. It is not clear whether the predictive accuracy for the emitter temperature would persist for other operating conditions given the sparsity of experimental data.

We do not have an experimental standard for comparison with the orifice results, though we may be able to identify unreasonable predictions. For example, Mandell and Katz's orifice model seems to over predict both plasma density and ionization fraction, a possible consequence of the omission of the 5/2 factor in the plasma power balance. We show in Table 5 the impact of this correction to the convective term.

		Siegfried and Wilbur	Goebel and Katz	Experiment (average)
TH8	n_e ($\times 10^{-20}$ m^{-3})	3.3	4.0	3.6
	T_{eV} (eV)	1.4*	1.6	1.4
	ϕ_p (V)	10.0	9.2*	9.2
	ϕ_s (V)	–	5.7	–
	T_c (K)	1,420	–	1,470†
	L_{emit} (mm)	1.9	6.0*	6.0
	α (%)	1.2	3.3	3.7
TH15	n_e ($\times 10^{-20}$ m^{-3})	11.9	2.8	4.7
	T_{eV} (eV)	1.4*	1.5	1.4
	ϕ_p (V)	14.7	5.5*	5.5
	ϕ_s (V)	–	2.8	–
	T_c (K)	1,530	–	1,540†
	L_{emit} (mm)	0.49	6.0*	6.0
	α (%)	1.7	1.8	2.7

* Model input.

† Calculated from fits to measured temperature profiles — $T_c = 1191.6 I_d^{0.0988}$

Table 4. Results from the insert models applied to the NSTAR discharge cathode. The experimental data is spatially averaged from data reported in Ref. 65. Plasma potential accuracy is ±1 V, and electron temperature ±0.5 eV. No information about accuracy of density measurements is reported.

		Mandell and Katz	Mandell and Katz (with correction)	Mizrahi *et al.*	Goebel and Katz
TH8	n_e ($\times 10^{-20}$ m^{-3})	5.0	2.3	1.6	2.6
	T_{eV} (eV)	2.8	2.7	2.8	3.1
	α (%)	9.1	3.9	1.7	6.8
TH15	n_e ($\times 10^{-20}$ m^{-3})	13.5	7.6	4.4	6.8
	T_{eV} (eV)	2.7	2.5	2.7	2.9
	α (%)	18.6	9.3	4.2	6.0

Table 5. Results from the orifice models applied to the NSTAR discharge cathode.

IV. Critical Issues

A. The neutral flow question

The 0-D models outlined in the preceding sections rely on some form of neutral flow model — either empirical, Poiseuille, or isentropic quasi-1D flow. However, both the presence of plasma and high-temperature insert walls introduces a non-negligible source of heat addition which violates the assumptions of both Poiseuille

and isentropic flow models. More importantly, the Poiseuille flow is invalid in the region near the orifice inlet — a constriction — and in the region near the orifice outlet — an expansion to vacuum. Table 6 and Fig. 22 present the pressure as a function of discharge current and mass flow rate, calculated using various flow models, for both the NSTAR discharge cathode, and the NEXIS discharge cathode, respectively. The NSTAR and NEXIS dimensions are shown in Table 2. A constant neutral gas temperature of $4,000$ K is assumed for the Poiseuille and isentropic flow calculations.

Operating condition		Pressure model			Experiment
		Empirical correlation	Poiseuille	Modified Poiseuille	
TH4	$I_d = 5.95$ A $\dot{m} = 2.47$ sccm	5.6	5.7	5.6	4.0
TH8	$I_d = 8.24$ A $\dot{m} = 2.47$ sccm	7.1	5.7	5.6	4.6
TH12	$I_d = 9.9$ A $\dot{m} = 2.81$ sccm	9.4	6.0	6.1	5.9
TH15	$I_d = 13.3$ A $\dot{m} = 3.7$ sccm	15.9	6.8	7.1	8.1

Table 6. Comparison of pressure predictions (in Torr) of multiple flow models applied to the NSTAR cathode. Experimental data is taken from Ref.66 for TH4, TH8, and TH15, and from Ref. 67 for TH12.

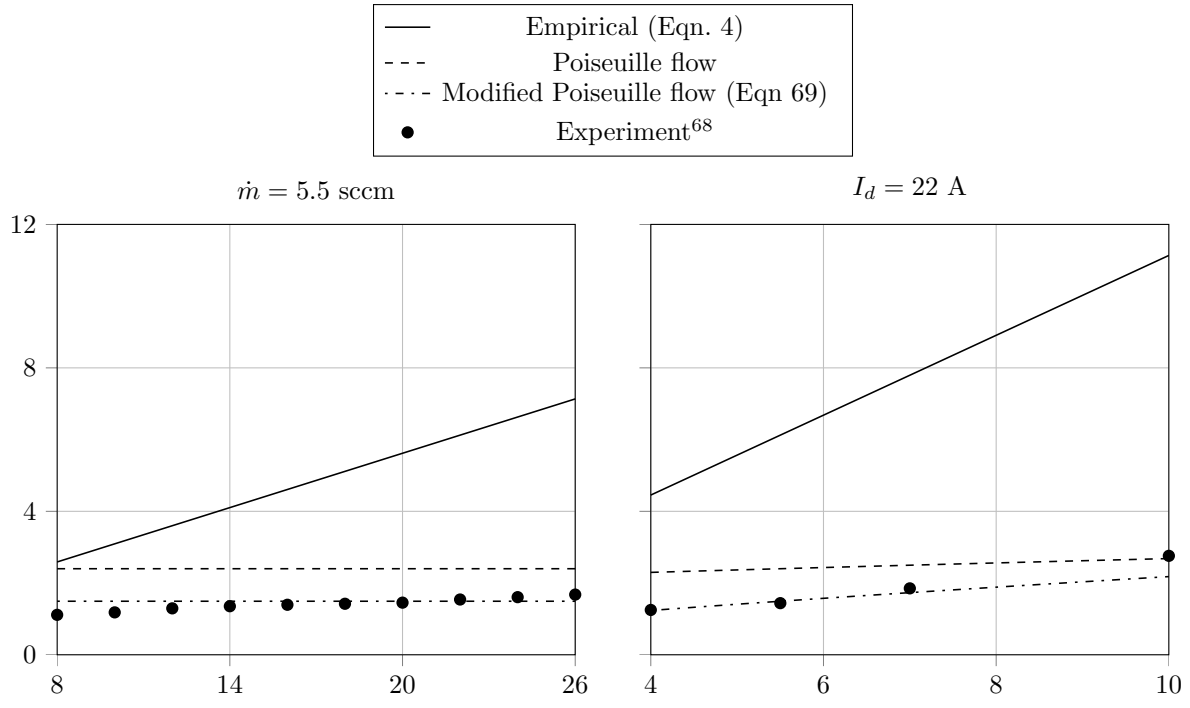

Figure 22. Comparison of pressure prediction from multiple flow models applied to the NEXIS cathode. Left: constant mass flow rate $\dot{m} = 5.5$ sccm. Right: constant discharge current $I_d = 22$ A. Experimental data from Ref. 68.

Only the empirical model predicts any variation in the cathode pressure with discharge current. However, Siegfried and Wilbur's correlation clearly does not generalize to other cathodes, and overestimates the pressure in both the NSTAR and NEXIS. A more general correlation seems to be necessary for this approach to produce accurate results, as the empirical models of Capacci *et al.* and Siegfried and Wilbur do not include variation in orifice length. These formulations also assume scaling that conforms to isentropic flow conditions.

The modified Poiseuille flow model used by Domonkos and Albertoni *et al.* produces acceptable results for the NEXIS, though the accuracy decreases as the mass flow rate increases. The results for the same model

applied to the NSTAR cathode differ by an average value of over 20% from the experimental results. The departure of the modified Poiseuille flow results from those of standard Poiseuille flow is not significant at low mass flow rates. Use of the Poiseuille flow model with choked flow as a downstream boundary condition may also be fundamentally inconsistent, as the average velocity calculated from the linearized pressure gradient is not necessarily equivalent to the (constant) sonic velocity. Without heat addition or viscous contributions, the velocity within the orifice should be assumed constant, as it is a function of only the channel size.

B. Flux calculations

The coefficients preceding flux terms in several of the model power balances are used inconsistently, the correct term scalings are given below.

CONVECTION The $5/2T_{eV}I_d$ term that appears in the 0D plasma volume power balances is a result of the integral form of the energy equation. As shown in Table 5, inappropriately rescaling this factor has a significant effect on model results. In steady-state, neglecting viscosity, kinetic-energy terms, and collisions, the energy equation simplifies to

$$\nabla \cdot \left(\frac{5}{2} T_{eV} n_e e \boldsymbol{u}_e + \boldsymbol{q}_e \right) = -e n_e \boldsymbol{E} \boldsymbol{u}_e. \tag{139}$$

The first term on the left-hand side corresponds to the convection of energy at the fluid velocity. A direct integration of this term over a volume along with the application of Gauss' law yields the correct expression for the convected energy.

RANDOM FLUX A derivation of the average energy of an electron leaving the volume to a surface may be found in Ref. 42, Appendix C in Ref. 11, or Ref. 63. The $2T_{eV}$ term stems from the assumed Maxwellian distribution crossing a surface. The average energy is higher than the average energy per particle in the volume due to higher-energy particles escaping the volume at a greater rate. The average energy is obtained by computing the ratio of the energy flux to the wall to the total particle flux. For a Maxwellian distribution, the total particle flux is given by,

$$\Gamma = \frac{n\bar{c}}{4}, \tag{140}$$

where $\bar{c}$ is the distribution-averaged velocity. The energy flux is given by:

$$\Gamma_e = \frac{n\bar{c}}{4} 2T_{eV}. \tag{141}$$

C. Sheath considerations

It appears that one of the primary reasons that the described models begin to lose accuracy outside of the domain of operating conditions for which they were developed is their handling of the sheath and plasma potential structure. The models generally choose from one of the following idealizations: a purely 0-D sheath (no variation in n_e anywhere), a mostly 0-D model with a flat potential structure in the plasma bulk but where an attempt has been made to include some or all of the effects of the pre-sheath, or an ambipolar diffusion model.

1. Flat potential profile

In all variants of Siegfried and Wilburs's model and in that of Capacci *et al.*, no attempt was made to account for the variation of plasma density induced by the sheath/pre-sheath, and, in accordance with a strict 0-D assumption, the plasma density and potential are assumed constant within the entire control volume. The only advantage of this approach is its simplicity; due to the collisionality and current densities present within the cathode, it is unlikely that all of the potential drop from the cathode centerline to the emitter surface would be translated into ion bombardment energy or emitted electron energy. This approach artificially decreases the backstreaming electron flux reaching the emitter surfaces, as shown in Figure 3, and this term is wrongfully neglected by the authors that use this type of sheath model. Finally, this model also causes the over prediction of the plasma potential, as the ion bombardment power must increase in order to provide sufficient heating to the insert for self-sustaining operation.

2. Flat potential profile with pre-sheath

In the models of Domonkos and Albertoni *et al.*, the plasma potential is assumed to differ from the sheath potential by $T_e/2$, the potential drop due the Bohm condition at the sheath edge. The associated energy term is often neglected (therefore ϕ_s is essentially ϕ_p), with the primary contribution to the model being the modification of the plasma density used to calculate fluxes to the insert surface. This idealization does little to alleviate the issues of the purely 0-D sheath model described above.

3. Ambipolar diffusion model

The model used by Gobel and Katz[11] includes density variation in the radial direction. It is the only implementation of a sheath voltage that is independent of the plasma potential. The diffusion equation solved, however, assumes no variation in the axial direction (consistent with the 0-D approach) and *zero* plasma density at the "wall" of the insert or orifice plasma region. This wall boundary condition is problematic; in the aforementioned model, the sheath is assumed to have zero thickness, and therefore the sheath edge coincides with the "wall" for the purposes of the ambipolar diffusion model. Depending on the channel geometry and pressure, it may be reasonable to assume that the plasma density is negligible at the sheath edge compared to the bulk plasma density, but for other conditions (especially small diameters and low pressures) this would introduce significant error. This is discussed in greater detail in Section II.F. This model also leads to the over prediction of the electron temperature, which in turn affects the power balance used to calculate the sheath voltage. As mentioned in Ref. 43, this ambipolar diffusion model is also not appropriate for application to the orifice region plasma. The global power balance method used to calculate the sheath voltage also predicts negative values of ϕ_s, or values of ϕ_s greater than the input ϕ_p, for some operating conditions.

V. Conclusion

We have reviewed zero-dimensional orificed hollow cathode models developed in the past 40 years that are relevant for electric propulsion applications. Our intent is to provide critical information with regards to the validity and to the consequences of the assumptions made, and the range of applicability of each model. We performed term-by-term comparisons of the physical equations proposed when necessary, re-implemented the models when possible, and compared our implementations to the original authors' calculations. We applied the models to two different cathodes with available experimental data, and found them to be generally unable to produce good agreement with experiment. For orifice models, the lack of experimental measurements within the orifice region make it difficult to assess model accuracy.

Common issues include the modeling of the neutral gas flow through the cathode and orifice, the calculation of convection losses, and the representation of the potential or density structure within the 0D volume. We argue that the neutral gas flow is treated inappropriately and that new or revised models appear necessary to predict the cathode pressure accurately.The assumptions of existing flow models are generally incompatible with cathode environments. We present calculations for the energy flux terms, and discuss the different approaches that were used to treat the radial variation of the plasma and sheath potentials inside the cathode. It is apparent that the inconsistencies or simplifications inherent in the proposed sheath models affect their accuracy and ability to generalize to other operating conditions. In order to develop a plasma and sheath model with general predictive capability, proper boundary conditions and self-consistent approaches are likely needed.

References

[1]Brown, D. L., et al., "Air Force Research Laboratory High Power Electric Propulsion Technology Development," *IEEE Aerospace Conference*, 2009.

[2]Goebel, D. M. and Chu, E., "High Current Lanthanum Hexaboride Hollow Cathodes for High Power Hall Thrusters," *32nd International Electric Propulsion Conference*, 2011.

[3]Hofer, R.R., et al., "Evaluation of a 4.5 kW Commercial Hall Thruster System for NASA Science Missions," *42nd AIAA/ASME/SAE/ASEE Joint Propulsion Conference & Exhibit*, 2006.

[4]Plasek, M. L., et al., "Experimental Investigation of a Large-Diameter Cathode," *50th AIAA/ASME/SAE/ASEE Joint Propulsion Conference & Exhibit*, 2014.

[5]Goebel, D. M. and Chu, E., "High-Current Lanthanum Hexaboride Hollow Cathode for High-Power Hall Thrusters," *Journal of Propulsion and Power*, 2014.

[6]Hall, S., et al., "Implementation and Initial Validation of a 100-kW Class Nested-Channel Hall Thruster," *50th AIAA/ASME/SAE/ASEE Joint Propulsion Conference & Exhibit*, 2014.

[7]Wordingham, C. J., et al., "Multiple-Kilowatt-Class Graphite Heater for Large Hollow Cathode Ignition," *51st AIAA/ASME/SAE/ASEE Joint Propulsion Conference & Exhibit*, 2015.

[8]Shastry, R., et al., "Status of NASAs Evolutionary Xenon Thruster (NEXT) Long-Duration Test as of 50,000 h and 900 kg Throughput," *33rd International Electric Propulsion Conference*, 2013.

[9]Albertoni, R., *Cathode Processes in MPD Thrusters*, Ph. d., Universita Degli Studi di Pisa, 2012.

[10]Siegfried, D. E. and Wilbur, P. J., "A model for mercury orificed hollow cathodes-Theory and experiment," *AIAA journal*, Vol. 22, No. 10, 1984, pp. 1405–1412.

[11]Goebel, D. and Katz, I., *Fundamentals of Electric Propulsion: Ion and Hall Thrusters*, John Wiley & Sons, Inc., 2008.

[12]Siegfried, D. E. and Wilbur, P. J., "Phenomenological Model Describing Orificed , Hollow Cathode Operation," *AIAA Journal*, Vol. 21, No. 1, 1983, pp. 5–6.

[13]Domonkos, M. T., *Evaluation of low-current orificed hollow cathodes*, Ph.d., University of Michigan, 1999.

[14]Albertoni, R., Pedrini, D., Paganucci, F., and Andrenucci, M., "A Reduced-Order Model for Thermionic Hollow Cathodes," *IEEE Transactions on Plasma Science*, Vol. 41, No. 7, 2013, pp. 1731–1745.

[15]Prewett, P. and Allen, J., "The double sheath associated with a hot cathode," *Proceedings of the Royal Society of London A: Mathematical, Physical and Engineering Sciences*, Vol. 348, The Royal Society, 1976, pp. 435–446.

[16]Wilbur, P. J., "Advanced Ion Thruster Research," Tech. Rep. CR-168340, NASA, 1984.

[17]van der Walt, S., Colbert, C. S., and Varoquaux, G., "The NumPy Array: A Structure for Efficient Numerical Computation," *Computing in Science & Engineering*, Vol. 13, 2011, pp. 22–30.

[18]Jones, E., Oliphant, T., Peterson, P., et al., "SciPy: Open source scientific tools for Python," 2001–, Online.

[19]More, J. J., Garbow, B. S., and Hillstrom, K. E., "User guide for MINPACK-1," Tech. Rep. ANL-80-74, Argonne National Laboratory, 1980.

[20]Siegfried, D. and Wilbur, P. J., "An investigation of mercury hollow cathode phenomena," *13th International Electric Propulsion Conference*, 1978.

[21]Beßling, H., "Theorie der Hochtemperatur-Hohlkathode, ein Modell für den Kathodenmechanismus," Tech. rep., DFVLR - Institut fur Energiewandlung und Elektrische Antriebe, 1976, (In German).

[22]Siegfried, D. E. and Wilbur, P. J., "Studies on an experimental quartz tube hollow cathode," *14th International Electric Propulsion Conference*, 1979.

[23]Siegfried, D. E., *A Phenomenological Model for Orificed Hollow Cathodes*, Ph.d., Colorado State University, 1982.

[24]Domonkos, M. T., "A Particle and Energy Balance Model of the Orificed Hollow Cathode," *38th AIAA/ASME/SAE/ASEE Joint Propulsion Conference & Exhibit*, 2002.

[25]Mandell, M. J. and Katz, I., "Theory of Hollow Cathode Operation in Spot and Plume Modes," *30th AIAA/ASME/SAE/ASEE Joint Propulsion Conference & Exhibit*, 1994.

[26]Katz, I., Gardner, B., Jongeward, G., Patterson, M., and Myers, R., "A model of plasma contactor behavior in the laboratory," *34th Aerospace Sciences Meeting and Exhibit*, 1996.

[27]Katz, I., Gardner, B. M., Mandell, M. J., Jongeward, G. A., Patterson, M., and Myers, R. M., "Model of Plasma Contactor Performance," *Journal of Spacecraft and Rockets*, Vol. 34, No. 6, 1997.

[28]Katz, I., Mandell, M. J., Patterson, M., and Domonkos, M., "Sensitivity of Hollow Cathode Performance to Design and Operating Parameters," *35th AIAA/ASME/SAE/ASEE Joint Propulsion Conference & Exhibit*, 1999.

[29]Hayashi, M., "Determination of Electron-Xenon Total Excitation Cross-Sections, from Threshold to 100 eV, From Experimental Values of Townsend's alpha," *Journal of Physics D: Applied Physics*, Vol. 16, 1983, pp. 581–589.

[30]"Hayashi database," `http://www.lxcat.net`, Retrieved on Jun. 17, 2017.

[31]Hayashi, M., "Bibliography of Electron and Photon Cross Sections with Atoms and Molecules Published in the 20th Century - Xenon," Tech. Rep. NIFS-DATA-79, NIFS, 2003.

[32]Capacci, M., Minucci, M., and Severi, A., "Simple numerical model describing discharge parameters in orificed hollow cathode devices," *33rd AIAA/ASME/SAE/ASEE Joint Propulsion Conference & Exhibit*, 1997.

[33]Mikellides, I. G., Katz, I., Goebel, D. M., Jameson, K. K., and Polk, J. E., "Wear Mechanisms in Electron Sources for Ion Propulsion, I: Neutralizer Hollow Cathode," *Journal of Propulsion and Power*, Vol. 24, No. 4, 2008, pp. 855–865.

[34]Langmuir, I., "The interaction of electron and positive ion space charges in cathode sheaths," *Physical Review*, Vol. 33, No. 6, 1929, pp. 954–989.

[35]Raadu, M. A., "The physics of double layers and their role in astrophysics," *Physics Reports*, Vol. 178, No. 2, 1989, pp. 25–97.

[36]Wei, R. and Wilbur, P. J., "Space-charge-limited current flow in a spherical double sheath," *Journal of Applied Physics*, Vol. 60, No. 7, 1986, pp. 2280–2284.

[37]Korkmaz, O. and Celik, M., "Global numerical model for the assessment of the effect of geometry and operation conditions on insert and orifice region plasmas of a thermionic hollow cathode electron source," *Contributions to Plasma Physics*, Vol. 54, No. 10, 2014, pp. 838–850.

[38]Huba, J. D., "NRL Plasma Formulary," NRL/PU/6790, 2011.

[39]"Double-Ion Production in Mercury Thrusters," Tech. Rep. CR-135019, NASA, 1976.

[40]Williams, G. J., Smith, T. B., Domonkos, M. T., Shand, K. J., Gallimore, A. D., and Drake, R. P., "Laser Induced Fluorescence Characterization of Ions Emitted from Hollow Cathodes," *35th AIAA/ASME/SAE/ASEE Joint Propulsion Conference & Exhibit*, 1999.

[41]"SIGLO database," `http://www.lxcat.net`, Retrieved on Jun. 17, 2017.

[42]Jones, T. J., *Thermionic emission*, Methuin ltd., 1936.

[43]Katz, I., Anderson, J. R., Polk, J. E., and Brophy, J. R., "One-Dimensional Hollow Cathode Model," *Journal of Propulsion and Power*, Vol. 19, No. 4, 2003, pp. 595–600.

[44]Miller, J. S., Pullins, S. H., Levandier, D. J., Chiu, Y. H., and Dressler, R. A., "Xenon charge exchange cross sections for electrostatic thruster models," *Journal of Applied Physics*, Vol. 91, No. 3, 2002, pp. 984–991.

[45]Hause, M., Prince, B., and Bemish, R., "Krypton charge exchange cross section for Hall effect thruster models," *Journal of Applied Physics*, Vol. 113, 2013.

[46]Mizrahi, J. P., Vekselman, V., Krasik, Y., and Gurovich, V., "0-D Plasma Model for Orificed Hollow Cathodes," *32nd International Electric Propulsion Conference*, 2011.

[47]Mizrahi, J., Vekselman, V., Gurovich, V., and Krasik, Y. E., "Simulation of Plasma Parameters During Hollow Cathodes Operation," *Journal of Propulsion and Power*, Vol. 28, No. 5, 2012, pp. 1134–1137.

[48]Katz, I., Anderson, J., Polk, J., and Brophy, J., "A Model of Hollow Cathode Plasma Chemistry," *38th AIAA/ASME/SAE/ASEE Joint Propulsion Conference & Exhibit*, 2002.

[49]Pedrini, D., Albertoni, R., Paganucci, F., and Andrenucci, M., "Theoretical Model of a Lanthanum Hexaboride Hollow Cathode," *IEEE Transactions on Plasma Science*, Vol. 43, No. 1, 2015.

[50]Pedrini, D., Cannelli, F., Ducci, C., Misuri, T., Paganucci, F., and Andrenucci, M., "Hollow Cathodes Development at SITAEL," *Space Propulsion*, 2016.

[51]Coletti, M. and Gabriel, S. B., "Insert Temperature Measurements of a 180A Hollow Cathode for the HiPER Project," *48th AIAA/ASME/SAE/ASEE Joint Propulsion Conference & Exhibit*, 2012.

[52]Polk, J. E., Goebel, D. M., and Guerrero, P., "Thermal Characteristics of a Lanthanum Hexaboride," *34th International Electric Propulsion Conference*, 2015.

[53]Krishnan, M., Jahn, R. G., von Jaskowsky, W. F., and Clark, K. E., "Physical processes in hollow cathode discharge," *AIAA Journal*, Vol. 15, No. 9, 1977, pp. 1217–1223.

[54]Chang, C. H. and Pfender, E., "Nonequilibrium modeling of low-pressure argon plasma jets; Part I: Laminar flow," *Plasma Chemistry and Plasma Processing*, Vol. 10, No. 3, 1990, pp. 473–491.

[55]Stiel, L. I. and Thodos, G., "The Viscosity of Nonpolar Gases at Normal," *A.I.Ch.E. Journal*, Vol. 7, No. 4, 1961, pp. 611–615.

[56]McQuarrie, D. A., *Statistical Mechanics*, Harper's Chemistry Series, 1976.

[57]Hirschfelder, J. O., Curtiss, C. F., and Bird, R. B., *Molecular Theory of Gases and Liquids*, Wiley, 1954.

[58]Goebel, D., Jameson, K. K., Watkins, R. M., and Katz, I., "Hollow Cathode and Keeper-Region Plasma Measurements Using Ultra-Fast Miniature Scanning Probes," *40th AIAA/ASME/SAE/ASEE Joint Propulsion Conference & Exhibit*, 2004.

[59]Katz, I., Polk, J. E., Mikellides, I. G., Goebel, D. M., and Hornbeck, S. E., "Combined Plasma and Thermal Hollow Cathode Insert Model," *29th International Electric Propulsion Conference*, 2005.

[60]Mikellides, I. G., Katz, I., Goebel, D. M., Polk, J. E., and Jameson, K. K., "Plasma processes inside dispenser hollow cathodes," *Physics of Plasmas*, Vol. 13, 2006.

[61]Mikellides, I. G., Katz, I., Goebel, D. M., Jameson, K. K., and Polk, J. E., "Wear Mechanisms in Electron Sources for Ion Propulsion, II: Discharge Hollow Cathode," *Journal of Propulsion and Power*, Vol. 24, No. 4, 2008, pp. 866–879.

[62]Mikellides, I. G., Katz, I., Goebel, D. M., and Polk, J. E., "Model of a Hollow Cathode Insert Plasma," *40th AIAA/ASME/SAE/ASEE Joint Propulsion Conference & Exhibit*, 2004.

[63]Mikellides, I. G., Katz, I., Goebel, D. M., and Polk, J. E., "Hollow cathode theory and experiment. II. A two-dimensional theoretical model of the emitter region," *Journal of Applied Physics*, Vol. 98, No. 2005, 2005.

[64]Goebel, D. M., Jameson, K. K., Watkins, R. M., Katz, I., and Mikellides, I. G., "Hollow cathode theory and experiment. I. Plasma characterization using fast miniature scanning probes," *Journal of Applied Physics*, Vol. 98, No. 11, 2005, pp. 1–9.

[65]Jameson, K. K., Goebel, D. M., and Watkins, R. M., "Hollow Cathode and Keeper-Region Plasma Measurements," *41st AIAA/ASME/SAE/ASEE Joint Propulsion Conference & Exhibit*, 2005.

[66]Rawlin, V., Sovey, J., Anderson, J., and Polk, J., "NSTAR flight thruster qualification testing," *34th AIAA/ASME/SAE/ASEE Joint Propulsion Conference & Exhibit*, 1998.

[67]Tighe, W.G., et al., "Hollow Cathode Ignition and Life Model," *41st AIAA/ASME/SAE/ASEE Joint Propulsion Conference & Exhibit*, 2005.

[68]Jameson, K. K., Goebel, D. M., and Watkins, R. M., "Hollow Cathode and Thruster Discharge Chamber Plasma Measurements Using High-Speed Scanning Probes," *29th International Electric Propulsion Conference*, 2005.

Appendices

A. Summary of 0D Models

Model	Inputs		Outputs	Reference(s)
Siegfried and Wilbur	Geometry	r_o	α, n_e	20
	Gas	ϵ_i, Σ_i/Σ_0		
	Plasma / Experimental	T_{eV}		
	Operating conditions	$T_c = T_g$, $\dot{m}$ or P		
Siegfried and Wilbur	Geometry	r_o, r_c	n_e, n_g, ϕ_p, $T_c = T_g$	10, 12, 23
	Gas	ϵ_i, M		
	Emitter	ϕ_w, D_{RD}		
	Plasma / Experimental	T_{eV}		
	Operating conditions	I_d, and $\dot{m}$ or P		
	Other	$\dot{q}_{th}$, c_1 , c_2 , c_3		
Mandell and Katz	Geometry	r_o, L_o	n_e, n_g, T_{eV}	26–28, 48
	Gas	ϵ_i, ϵ_{ex}, M, σ_{iz} σ_{ex}, ν_{en}, ν_{ei}		
	Plasma / Experimental	T_{eV}^{ins}, T_{gV}		
	Operating conditions	I_d, $\dot{m}$		
Goebel and Katz	Geometry	r_o, r_c, L_o	$(n_e\,, n_g\,, T_{eV}\,, \phi_s)_{\text{insert}}$ $(n_e\,, T_{eV}\,, n_g)_{\text{orifice}}$	11, 43
	Gas	ϵ_i, μ, M, σ_{iz} σ_{CEX},ν_{en}, ν_{ei}		
	Emitter	ϕ_w, D_{RD}		
	Plasma / Experimental	ϕ_p, T_{gV} or T_c, L_{emit}		
	Operating conditions	I_d, $\dot{m}$		
Mizrahi *et al.*	Geometry	r_o, L_o	n_e, n_g, T_{eV}	46, 47
	Gas	ϵ_i, ϵ_{ex}, μ, M, σ_{iz} σ_{ex}, σ_{CEX},ν_{en}, ν_{ei}		
	Plasma / Experimental	T_{eV}^{ins} , $T_{iV} = T_{gV}$		
	Operating conditions	I_d, $\dot{m}$		
	Free parameter	δ		

Table 7: List of reviewed and re-implemented models with required inputs and outputs.

A. Equation list — Siegfried and Wilbur

Physical Basis	Equation
Choked orifice flow	$P = \frac{\dot{m}\sqrt{T_g}}{\pi r_o^2}\left(\frac{\gamma}{R}\left(\frac{2}{\gamma+1}\right)^{\frac{\gamma+1}{\gamma-1}}\right)^{-1/2}$
Two-temperature Saha equation	$\frac{\alpha^{1+\tau_{ge}}}{(1-\alpha)^{\tau_{ge}}(1+\alpha/\tau_{ge})} = \frac{1}{P}\frac{(2\pi m)^{3/2}}{h^3}e^{5/2}T_{gV}T_{eV}^{3/2}\left(\frac{\Sigma_i}{\Sigma_0}\right)^{\tau_{ge}}\exp\left(-\frac{\epsilon_i}{T_{eV}}\right)$
Perfect gas law	$P = e\left(n_e T_{eV} + n_g T_{gV} + n_i T_{iV}\right)$

Table 8. List of Equations for model from Ref. 20

Physical Basis	Equation
Main Equations	
Perfect gas law	$P = e\left(n_e T_{eV} + n_g T_{gV} + n_i T_{iV}\right)$
Current Balance	$I_d = I_e + I_i = J_{em}A_{\text{emit}} + J_i A_s$
Insert surface Power Balance	$J_i A_{\text{emit}}\left(\phi_p + \epsilon_i - \phi_w\right) = \dot{q}_{th} + I_e\phi_{\text{eff}}$
Plasma Power Balance	$\phi_p I_e = \epsilon_i I_i + \frac{5}{2}T_{eV}I_d$
Supporting Equations	
Empirical	$P = \left(\frac{4\dot{m}}{r_o^2}\right)\left(c_1 + c_2 I_d\right)\times 10^{-3}$
Bohm Criterion	$J_i = en_e\left(\frac{eT_{eV}}{M}\right)^{1/2}$
Richardson-Dushman equation	$J_{em} = D_{RD}T_c^2\exp\left(-\frac{e\phi_{\text{eff}}}{k_B T_c}\right)$
Schottky effect	$\phi_{\text{eff}} = \phi_p - \left(\frac{e\lvert E_c\rvert}{4\pi\epsilon_0}\right)^{1/2}$
Double-sheath Model	$E_c \approx \left(\frac{n_e e T_{eV}}{\epsilon_0}\right)^{1/2}\left(2\left(1+2\frac{\phi_p}{T_{eV}}\right)^{1/2} - 4\right)^{1/2}$
Emission length	$L_{\text{emit}} = c_3\lambda_{pr}$
Semi-empirical	$\lambda_{pr} = \left(\frac{6.5\times10^{-17}n_e}{\phi_p^2} + n_g\sigma_{in}\left(\phi_p\right)\right)^{-1}$

Table 9. List of Equations for model from Refs.10, 12, 16, 23.

The units are MKS, except for the empirical pressure correlation, where the mass flow rate is in equivalent-milliAmpères, pressure in Torr, and orifice radius in mm. For mercury, $n_g\sigma_{in}$ may be estimated with

$$n_g\sigma_{in} = \frac{10^3 n_g\phi_p}{2.83\times10^{23} - 1.5n_g}$$

Gas	c_1	c_2	c_3
Mercury	13.7	7.82	2
Argon	5.6	1.2	0.5
Xenon	9.0	4.0	0.5

Table 10. Constants necessary for model, for various gases.[16]

B. Equation list — Mandell and Katz

Physical Basis	Equation
Main Equations	
Mass conservation	$\dot{m} = \pi r_o^2 n_g e \sqrt{\frac{eT_{gV}}{2\pi M}} + \pi r_o^2 J_i$
Ion balance	$n_g \sigma_{iz}(T_{eV}) 4 J_e = 2\pi r_o \left(r_o + L_o\right) J_i$
Plasma power balance	$R_p I_d^2 = \left(\pi r_o^2 L_o\right) n_g (\sigma_{iz}\epsilon_i + \sigma_{ex}\epsilon_{ex}) J_e + I_d \left(T_{eV} - T_{eV}^{\text{ins}}\right)$
Supporting Equations	
Electron current density	$J_e = n_e e \sqrt{\frac{eT_{eV}}{2\pi m}}$
Ion current density	$J_i = n_e e \sqrt{\frac{eT_{eV}}{2\pi M}}$
Ionization cross-section	$\sigma_{iz} = 10^{-20} \cdot \left(3.97 + 0.643 T_{eV} - 0.0368 T_{eV}^2\right) \exp\left(-\epsilon_i / T_{eV}\right)$
Excitation cross-section	$\sigma_{ex} = 1.93 \times 10^{-19} T_{eV}^{-1/2} \exp\left(-11.6/T_{eV}\right)$
Plasma resistance	$R_p = \eta_p \frac{L_o}{\pi r_o}$
Plasma resistivity	$\eta_p = \frac{m}{n_e e^2} \left(\nu_{ei} + \nu_{en}\right)$
Electron-ion collision frequency (fully ionized plasma)	$\nu_{ei} = 2.9 \times 10^{-12} n_e T_{eV}^{-3/2} \ln \Lambda$
Coulomb logarithm	$\ln \Lambda = 30 - \frac{1}{2} \ln\left(n_e T_{eV}^{-3}\right)$
Electron-neutral collision frequency	$\nu_{en} = 6.6 \times 10^{-19} \frac{0.25 T_{eV} - 0.1}{1 + (0.25 T_{eV})^{1.6}} \sqrt{\frac{eT_{eV}}{m}} n_g$

Table 11. List of Equations for model from Ref.25–28, for xenon gas.

$\dot{m}$ has units of equivalent-Ampères in the mass conservation equation.

C. Equation list — Mizrahi *et al.*

Physical Basis	Equation
Main Equations	
Mass conservation	$\dot{m} = M\pi r_o^2 \left(\bar{n}_g + \bar{n}_e\right) \bar{u}_g$
Ion balance	$\bar{n}_g \sigma_{iz} \left(T_{eV}\right) \sqrt{\frac{8eT_{eV}}{\pi m}} = \frac{2D_a}{r_o^2} \left(1 + 2\left(r_o/L_o\right)^2\right)$
Plasma power balance	$RI_d^2 = \pi r_o^2 L_o \bar{n}_g \bar{n}_e e \bar{u}_e \left(\epsilon_i \sigma_{iz} + \epsilon_{ex} \sigma_{ex}\right) + \frac{5}{2}\left(T_{eV} - T_{eV}^{\text{ins}}\right) I_d$
Supporting Equations	
Poiseuille flow (incompressible)	$\bar{u}_g = \frac{1-\delta}{1+\delta} \frac{\bar{n}_g r_o^2}{4\mu L_o}$
Empirical viscosity	$\xi = 2.3 \times 10^{-5} \left(\frac{T_g}{289.7}\right)^{0.71 + 0.29 \cdot 289.7/T_g}$
Plasma parameter	$\Lambda = \frac{\lambda_D}{b_0}$
Impact parameter	$b_0 = \frac{e^2}{4\pi\epsilon_0 m \bar{u}_e^2}$
Electron-ion collision frequency (fully ionized plasma)	$\nu_{ei} = 2.9 \times 10^{-12} n_e T_{eV}^{-3/2} \ln \Lambda$
Electron-neutral collision frequency	$\nu_{en} = 6.6 \times 10^{-19} \frac{0.25T_{eV} - 0.1}{1 + (0.25T_{eV})^{1.6}} \sqrt{\frac{eT_{eV}}{m}} n_g$
Ion-neutral collision frequency	$\nu_{in} = \bar{n}_g \sigma_{\text{CEX}} \sqrt{\frac{eT_{iV}}{M}}$
Ambipolar diffusion coefficient	$D_a = \left(1 + \frac{T_{eV}}{T_{iV}}\right) \frac{eT_{iV}}{M\nu_{in}}$
Ionization cross-section	$\sigma_{iz} = 10^{-20} \cdot \left(3.97 + 0.643T_{eV} - 0.0368T_{eV}^2\right) \exp\left(-\epsilon_i/T_{eV}\right)$
Excitation cross-section	$\sigma_{ex} = 1.93 \times 10^{-19} T_{eV}^{-1/2} \exp\left(-11.6/T_{eV}\right)$
Plasma resistance	$R = \frac{L_o m}{\pi r_o^2 e^2 \bar{n}_e} \left(\nu_{ei} + \nu_{en}\right)$

Table 12. List of Equations for model from Ref. 46, 47, for xenon gas.